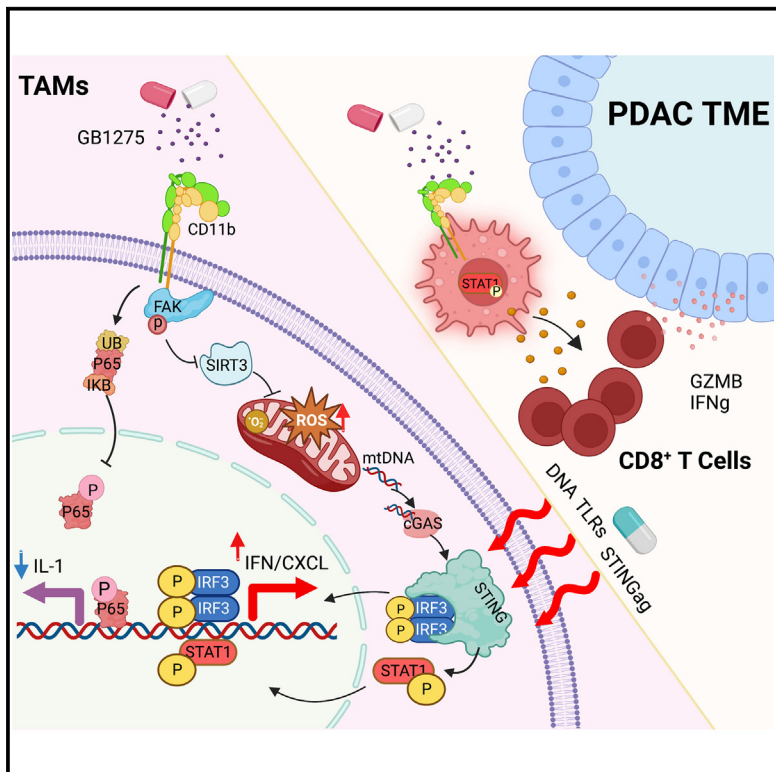


Context-dependent activation of STING-interferon signaling by CD11b agonists enhances anti-tumor immunity

Graphical abstract



Authors

Xiuting Liu, Graham D. Hogg,
Chong Zuo, ..., Haeseong Park,
Vineet Gupta, David G. DeNardo

Correspondence

ddenardo@wustl.edu

In brief

Liu et al. report that CD11b agonists activate STING/STAT/interferon pathways and represses NF-κB in *in vitro* systems, pancreatic cancer mouse models, and human tumors. Tumor cell death and innate immune agonists synergize with CD11b agonists, indicating potential mechanism-based therapeutic strategies for translation of CD11b agonist use in cancer patients.

Highlights

- CD11b agonists activates STING/STAT1 and represses of NF-κB in TAMs
- STING/pSTAT1 activation in TAMs enhances anti-tumor T cell immunity
- GB1275 increases pSTAT1 and STING in TAMs in patient tumor tissues
- Tumor cell death and innate immune agonists synergize with CD11b agonists

Article

Context-dependent activation of STING-interferon signaling by CD11b agonists enhances anti-tumor immunity

Xiuting Liu,¹ Graham D. Hogg,¹ Chong Zuo,¹ Nicholas C. Borcherding,² John M. Baer,¹ Varintra E. Lander,¹ Liang-I Kang,^{2,3} Brett L. Knolhoff,¹ Faiz Ahmad,¹ Robin E. Osterhout,⁴ Anna V. Galkin,⁴ Jean-Marie Bruey,⁴ Laura L. Carter,⁴ Cedric Mpoy,⁵ Kiran R. Vij,² Ryan C. Fields,^{3,5} Julie K. Schwarz,^{3,6,7} Haeseong Park,^{1,3} Vineet Gupta,⁸ and David G. DeNardo^{1,2,3,9,*}

¹Department of Medicine, Washington University School of Medicine, St. Louis, MO 63110, USA

²Department of Pathology and Immunology, Washington University School of Medicine, St. Louis, MO 63110, USA

³Siteman Cancer Center, Washington University School of Medicine, St. Louis, MO 63110, USA

⁴Gossamer Bio, Inc., San Diego, CA, USA

⁵Department of Surgery, Washington University School of Medicine, St. Louis, MO 63110, USA

⁶Department of Radiation Oncology, Washington University School of Medicine, St. Louis, MO 63110, USA

⁷Department of Cell Biology & Physiology, Washington University School of Medicine, St. Louis, MO 63110, USA

⁸Drug Discovery Center, Department of Internal Medicine, Rush University Medical Center, Chicago, IL, USA

⁹Lead contact

*Correspondence: ddenardo@wustl.edu

<https://doi.org/10.1016/j.ccr.2023.04.018>

SUMMARY

Chronic activation of inflammatory pathways and suppressed interferon are hallmarks of immunosuppressive tumors. Previous studies have shown that CD11b integrin agonists could enhance anti-tumor immunity through myeloid reprogramming, but the underlying mechanisms remain unclear. Herein we find that CD11b agonists alter tumor-associated macrophage (TAM) phenotypes by repressing NF- κ B signaling and activating interferon gene expression simultaneously. Repression of NF- κ B signaling involves degradation of p65 protein and is context independent. In contrast, CD11b agonism induces STING/STAT1 pathway-mediated interferon gene expression through FAK-mediated mitochondrial dysfunction, with the magnitude of induction dependent on the tumor microenvironment and amplified by cytotoxic therapies. Using tissues from phase I clinical studies, we demonstrate that GB1275 treatment activates STING and STAT1 signaling in TAMs in human tumors. These findings suggest potential mechanism-based therapeutic strategies for CD11b agonists and identify patient populations more likely to benefit.

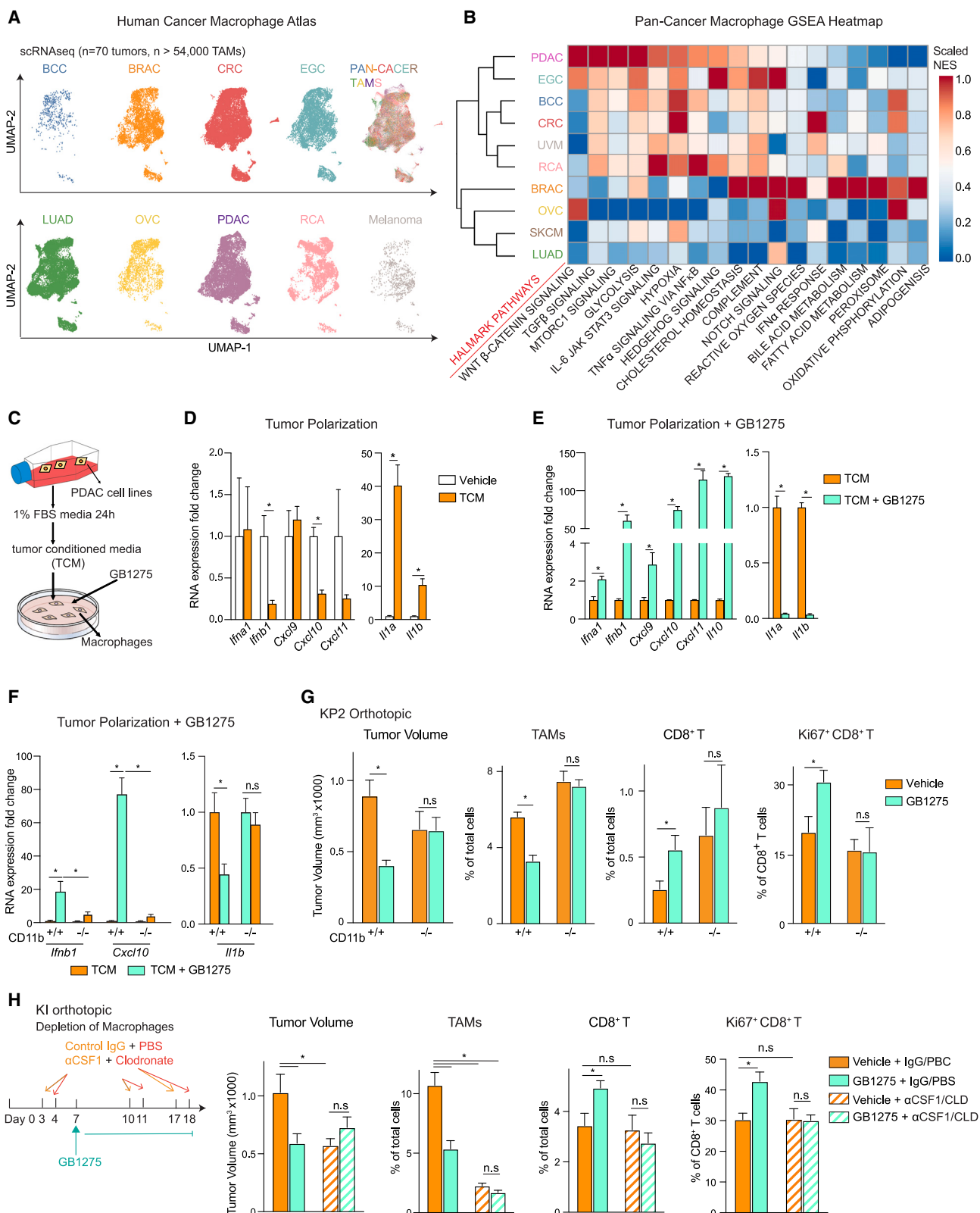
INTRODUCTION

The presence of high numbers of tumor-associated macrophages (TAMs) has been associated with poor clinical outcomes in many cancer types.¹ Despite this, TAMs harbor considerable plasticity and can play both pro-tumoral and anti-tumoral roles during therapy.² In some solid tumors such as pancreatic ductal adenocarcinoma (PDAC), dense desmoplastic and fibrotic stroma can drive immunosuppressive and wound healing programs in TAMs.^{3–5} Thus, reprogramming TAMs toward anti-tumor phenotypes is an attractive therapeutic strategy for such cancer types.⁶

TAMs are highly plastic to regulate multiple aspects of tumor promotion and restraint.^{1,2,7} Anti-tumorigenic macrophages are characterized by high expression of tumor necrosis factor alpha (TNF- α), interleukin-12a (IL-12a), inducible nitric oxide synthase, or MHC molecules, and T cell-attracting chemokines, such as CXCL9 and CXCL10.⁸ In contrast, pro-tumorigenic macro-

phages express high IL-10, the IL-1 decoy receptor, IL-1 receptor a (IL-1Ra), arginase-1, and the scavenger receptors CD163, CD204, or CD206.^{9,10} In human PDAC, TAMs are abundant in the tumor tissues of many patients.^{11,12} Some of the earliest approaches focused on TAM depletion. In preclinical models, blocking key chemokine receptors (e.g., CCR2 or CXCR1/2) or impairing TAM survival by inhibiting colony-stimulating factor-1 receptor (CSF1R) have slowed progression and improved responses to a variety of agents.^{13–15} However, these approaches tested to date have yet to achieve clinically significant benefits in solid tumors.¹⁴ This is likely because these myeloid-ablative strategies are subject to significant compensatory actions by untargeted subsets of myeloid cells that may ultimately limit their therapeutic efficacy in humans.^{14,16} An alternative strategy is to reprogram TAMs to support anti-tumor immunity.

Previous studies identified CD11b as a candidate target for immunotherapy.^{17–19} CD11b, composed of the α M (ITGAM) and β 2 (CD18) integrins, is widely expressed on multiple myeloid



(legend on next page)

cell subsets. Agonism of CD11b by small molecules modestly reduces the number of tumor-infiltrating immunosuppressive myeloid cells such as TAMs, monocytes, and granulocytes, and corresponds with an increase in T cell-mediated tumor control in PDAC and other mouse models.^{17–19} These data led to early-phase clinical testing in solid tumors (NTC04060342). In this study, we investigated the cellular and molecular mechanism by which CD11b agonists induce anti-tumor immunity and identified combination therapies to move forward.

RESULTS

Cancer-specific differences in TAM phenotypes

To understand the unique cancer-specific pathways in TAMs that may impair tumor immunity, we combined publicly available single-cell RNA sequencing (scRNA-seq) datasets from 70 tumors from 10 cancer types to identify ~54,000 TAMs. Even after integration, Uniform Manifold Approximation and Projection (UMAP) analysis still showed some segregation of TAMs by tumor types, suggesting the tumor-specific phenotypes and transcriptional features (Figure 1A). We next used gene set enrichment analysis (GSEA) to find cancer-specific phenotypic biases in TAMs. Comparing PDAC TAMs with TAMs in all other cancers, we observed some of the highest levels of the TGF- β , WNT, NF- κ B, and IL-4/IL-13 pathways and hypoxia and glycolysis gene sets (Figures 1B, S1A, and S1B). These results fit with the highly fibroinflammatory TME that is a hallmark of PDAC. We also observed strong congruence for these pathways across different databases (Figures S1A and S1B). In contrast, PDAC TAMs had some of the lowest levels of type-1 interferon signaling, antigen presentation, reactive oxygen species (ROS), and oxidative phosphorylation gene sets (Figures 1B, S1A, and S1B). Taken together, these data suggested that, in desmoplastic cancers, augmenting interferon and suppressing chronic inflammatory signaling may be key to unlocking tumor immunity.

The anti-tumor activity of CD11b agonists depends on TAMs

CD11b integrins can regulate both myeloid recruitment into inflamed tissues and cell phenotypes.¹⁷ In previous studies, CD11b agonists led to reduced tumor-infiltrating myeloid cells and restraint of tumor progression through indirect enhancement of T cell immunity.¹⁸ These small-molecule agonists were formerly named either LA1 or ADH503 but will be referred to as GB1275 herein, given their current clinical format (Figure S1C

and NTC04060342). Using *in vitro* systems, polarization of bone marrow-derived macrophages (BMDMs) with PDAC tumor cell-conditioned medium (TCM) led to reduced *Ifnb1* and *Cxcl10*, but increased *Il1* expression (Figures 1C and 1D). In contrast, adding GB1275 to TCM resulted in upregulation of *Ifna1*, *Ifnb1*, and *Cxcl9*, 10, and 11 but decreased *Il1a* and *Il1b* (Figures 1E, S1D, and S1E). These effects were lost in CD11b-null BMDMs (Figure 1F). *In vivo*, GB1275-treated PDAC tissue also showed increased CXCL10 and 11 and reduced IL-1 β (Figure S1F). Taken together, these data suggested CD11b agonism altered the effect of polarization by tumor-derived factors on TAMs. However, it remained unclear if TAM reprogramming was critical for efficacy *in vivo*.

To study this, we first confirmed that GB1275 exhibited anti-tumor activity *in vivo* through CD11b activation. A syngeneic PDAC cell line (KP2) derived from the genetic p48-Cre;LSL-Kras^{G12D};Trp53^{fl/fl} mice was orthotopically implanted in wild-type (WT) and CD11b-null mice. As expected, treatment of established tumors with GB1275 repressed PDAC progression, decreased TAM infiltration, and increased CD8 $^{+}$ T cell number and proliferation (Figures 1G and S1G–S1I). However, these effects were lost in CD11b-null mice (Figure 1G). As CD11b agonists could directly alter macrophage phenotype, we next determined if TAMs were critical for efficacy and anti-tumor immunity. We depleted tissue macrophages using a combination of anti-CSF1 IgGs and liposomal clodronate (α CSF1/CLD).²⁰ Mice bearing established syngeneic orthotopic tumors derived from Pdx1-Cre/LSL-Kras^{G12D}/Ink4a^{Fl/fl} mice (KI cells) were treated with α CSF1/CLD, which depleted >80% of TAMs, leading to reduced tumor progression (Figures 1H and S1J). GB1275 reduced KI tumor progression and increased CD8 $^{+}$ CTL infiltration and proliferation, but these effects were lost with TAM depletion (Figure 1H). Together, GB1275 activated CD11b on TAMs to drive anti-tumor immunity and restrain tumor growth.

CD11b-induced activation of TAMs improves T cell effector function

Previous studies showed that the anti-tumor activity of CD11b agonists was dependent on T cells.¹⁸ However, T cells seldom express CD11b. To eliminate potential direct effects on T cells, we assessed CD11b expression and direct impact of GB1275 on T cells. Analysis of p48-Cre;LSL-Kras^{G12D};Trp53^{fl/fl}(KPC) GEMMs, we found only 2%–4% of T cells expressed detectable CD11b, and even positive cells expressed >100-fold less than

Figure 1. GB1275 anti-tumor activity is dependent on TAM reprogramming

- (A) UMAP visualization of 54,000 TAMs from different cancer types, including PDAC, early gastric cancer (EGC), basal cell carcinoma (BCC), colorectal cancer (CRC), uveal melanoma (UVM), renal cancer (RCA), breast cancer (BRAC), ovarian serous cystadenocarcinoma (OVC), skin cutaneous melanoma (SKCM), and lung adenocarcinoma (LUAD). Clusters are annotated for cancer types.
- (B) GSEA-identified pathway enrichment in TAMs from each cancer type.
- (C) Schematic of *in vitro* macrophage system.
- (D) qPCR mRNA expression analysis of BMDMs treated with TCM for 6 h. Changes in gene expression are depicted as the fold change from the vehicle.
- (E and F) qPCR mRNA expression analysis of BMDMs isolated from wild-type (E) or CD11b-null mice (F) treated with TCM ± GB1275 for 7 h. Changes in gene expressions are depicted as the fold change from the vehicle.
- (G) WT or CD11b-null mice bearing syngeneic orthotopic KP2 tumors were treated with vehicle or GB1275 for 14 days. Tumor volume and frequencies of tumor-infiltrating TAMs, CD8 $^{+}$ T cells, and Ki67 $^{+}$ CD8 $^{+}$ T cells are depicted ($n = 6$ –8/group).
- (H) Mice bearing orthotopic KI tumors treated with IgG+ PBS or α CSF1 IgG+ clodronate as depicted. Tumor volume and frequencies of PDAC-infiltrating TAMs, CD8 $^{+}$ T cells, and Ki67 $^{+}$ CD8 $^{+}$ T cells at day 19 are depicted ($n = 7$ –9/group). All graphs depict the mean \pm SEM and * $p < 0.05$ using the two-sided t test. *In vitro* data are representative of three independent experiments. Also see Figure S1.

TAMs (Figure S2A), agreeing with previous human PDAC analysis.¹⁸ *In vitro*, GB1275 did not affect CD8⁺ T cell proliferation or effector cytokine production (Figures S2B and S2C). Together, CD11b agonists do not act directly on T cells.

To understand how T cell responses were changed, mass cytometry (CyTOF) was employed on orthotopic KI tumors (Figures 2A and 2B). UMAP analysis of CyTOF data on PDAC tissues identified several phenotypic subsets of CD8⁺ and CD4⁺ T cells (Figures 2C, 2D, and S2D). Across all CD8⁺ T cell subsets, we found that GB1275 increased granzyme B (GZMB) and Ki67 expressions (Figure 2E). Analyzing changes in CD8⁺ T cell subsets, we found that GB1275 increased proliferative effectors (cluster 5), expressing high levels of CD44, GZMB, T-bet, and Ki67, while CD103⁺ resident memory (cluster 2) and activated non-proliferative non-effector CD8⁺ T cells (cluster 3) were reduced (Figure 2F). Notably, across all subsets, we found a trend toward increased PD-1, CTLA-4, and TIM3 expression with treatment (Figure S2E). These data demonstrated that CD11b agonism-induced changes in myeloid cells drove CD8⁺ CTLs toward proliferative effector phenotypes. To further confirm this, we analyzed orthotopic KP2-OVA tumors (Figure 2G). Consistent with increased effector function, we also observed increased IFN-γ-positive and TNF-α/IFN-γ-double-positive CD8⁺ T cells in GB1275-treated PDAC tissues (Figures 2H and S2J). Together, these data suggest that CD11b agonists indirectly increase proliferative effector CD8⁺ T cells. By contrast, we observed only limited changes in CD4⁺ T cells (Figures S2F–S2I), which agreed with previous data, demonstrating that CD8⁺, but not CD4⁺ T cells, are required for CD11b agonist tumor control.¹⁸

CD11b agonism inhibits NF-κB signaling directly in TAMs

To understand how CD11b agonists changed TAM phenotype to support anti-tumor immunity, we performed scRNA-seq. We isolated CD45⁺ cells from syngeneic KP2 PDAC tissue from mice treated with vehicle or GB1275 for 14 days. UMAP analysis distinguished subsets of CD45⁺ cells (Figure S3A), from which we isolated TAMs/monocytes (Figure 3A). Reclustering of this population identified three subpopulations of TAMs and a monocyte cluster (Figures 3B and S3B). We next identified differentially expressed genes and conducted GSEA on the total TAM/monocyte populations. Consistent with CD11b integrin activation, we observed enrichment of integrin pathways in GB1275-treated TAMs (Figure 3C). In addition, oxidative phosphorylation and ROS signatures were also increased by GB1275 across all TAM subsets (Figures 3C and 3D). In contrast, inflammatory response and NF-κB signatures were decreased across all subsets of GB1275-treated TAMs (Figures 3C and 3D). At the gene level, the majority of NF-κB/IL-1 signature genes were decreased in TAMs from GB1275-treated mice (Figure 3E; Tables S1 and S2). Together, these data suggest that CD11b agonism alters TAM phenotypes *in vivo*.

Consistent with our *in vivo* observations, *in vitro*, GB1275 decreased expression of IL-1-associated genes, including *Il1a*, *Il1b*, *Il18*, and *Ccl2* in macrophages (Figure 3F), which was dependent on CD11b, but independent of the presence or sources of TCM (Figures S3C–S3E and S3F). We next assessed downregulation of NF-κB by GB1275 in BMDMs under standard

culture and with TCM. Under both conditions, GB1275 decreased total and phosphorylated NF-κB p65 and IκB protein levels (Figure 3G). Due to its known effect on IL-1 transcription,^{21,22} we focused on NF-κB. First, GB1275 lost its ability to decrease *Il1* when NF-κB p65 was silenced (Figures S3I–S3K). Next, we observed no decrease in NF-κB p65 mRNA by GB1275 (Figure S3H), suggesting that the regulation was likely through protein stability. To test this, we pretreated macrophages with MG132, a proteasome inhibitor, and found that GB1275 no longer decreased p65 protein (Figure 3H). Moreover, GB1275 increased poly-ubiquitination of p65 (Figure 3I), contributing to proteasomal degradation.^{23,24} Together, CD11b agonists induce p65 degradation to regulate NF-κB/IL-1 signaling.

To verify that CD11b agonists decreased NF-κB p65 *in vivo*, we performed multiplex immunohistochemistry (mIHC) analysis on PDAC tissues. We serially stained for p65, CD11b, F4/80, and cytokeratin (CK)-19 and found that GB1275 reduced the proportions of TAMs with nuclear p65⁺ (np65⁺) in KPC GEMM and orthotopic KP2 and KI tumors (Figures 3J–3L). Based on downregulated NF-κB/IL-1 signaling by GB1275 in our study, we next analyzed whether this signaling downregulation was related to favorable clinical outcomes in PDAC patients. To accomplish this, we identified a gene-set from the Hallmark NF-κB signaling pathway (GeneID = 7124) that was downregulated following GB1275 in TAMs in our scRNA-seq data (Figure 3E; Table S3). We then segregated PDAC patients from TCGA with this gene signature and found that low expression was indicative of better survival (Figure 3M). Similarly, lower *IL1* gene sets were indicative of better outcomes in PDAC patients (Figure S3O). These data suggest that CD11b agonist suppression of NF-κB/IL-1 signaling might lead to favorable clinical outcomes in patients.

CD11b agonists induce NF-κB inactivation in TAMs to inhibit inflammation but not IFN expression

We next tested if NF-κB or IL-1R was important for interferon induction or T cell enhancement. *In vitro*, GB1275's ability to increase *Ifn* genes in macrophages was independent of p65 expression (Figure S3L). *In vivo*, we treated PDAC-bearing mice with vehicle or GB1275 ± IL-1R blocking antibodies. As expected, IL-1R blockade slowed tumor progression and decreased immature monocyte and granulocyte infiltration (Figure S3M). However, GB1275's ability to improve CTL responses and tumor control was not dependent on IL-1R signaling (Figures S3M and S3N). Thus, CD11b agonist's downregulation of the NF-κB/IL-1 signaling contributed to dampening of inflammation, but not CTL-mediated tumor control.

CD11b agonists activate STING in TAMs

We next sought to understand how CD11b agonists induce *Ifn* genes in TAMs. *In vitro*, the induction of *Ifn* genes by GB1275 was dependent on TCM polarizing conditions but consistent across multiple cell line-derived TCMs (Figures 1E, 1F, and 4A). To investigate the signaling pathways involved, we performed reversed-phase protein array analyses on BMDMs treated with GB1275 ± TCM. After 4 and 7 h, GB1275 alone induced 20 and 36 protein changes (Figure S4A; Table S4). But, under TCM polarizing conditions, GB1275 induced greater than 60 protein changes at both timepoints, suggesting that

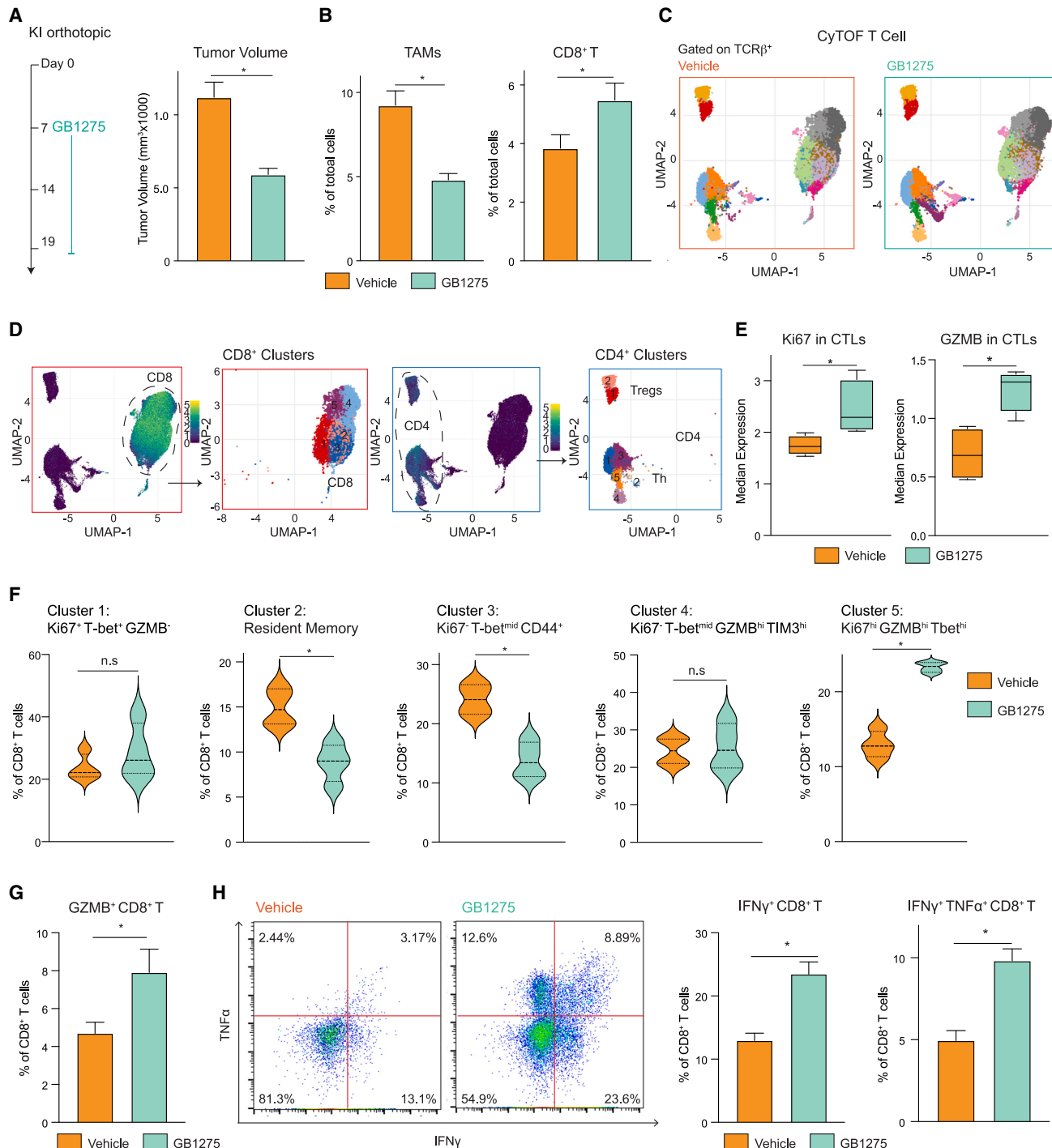
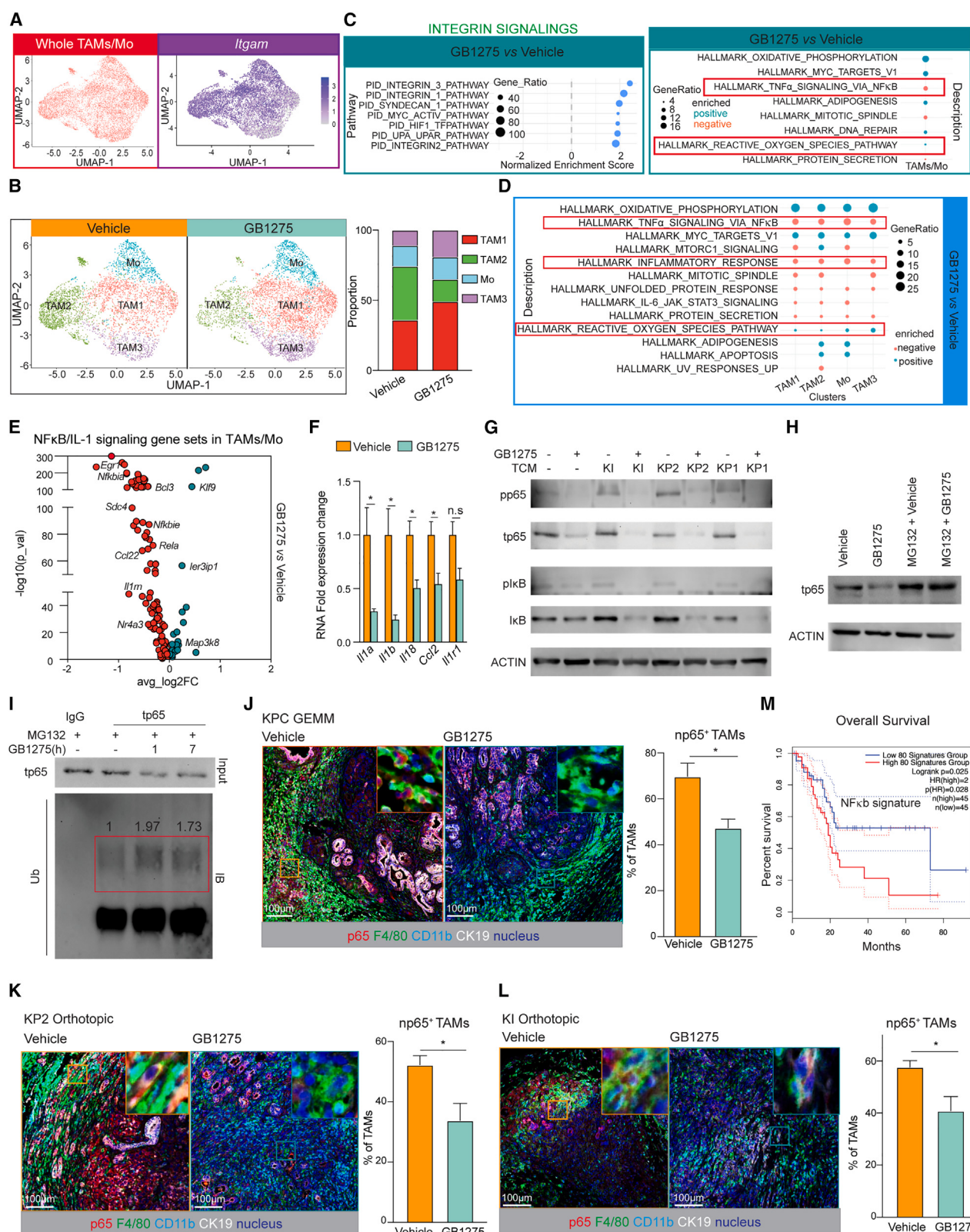


Figure 2. TAMs CD11b activation results in more proliferative effector T cells

- (A) Syngeneic KI orthotopic model and treatment (left). Tumor burden in each group (right) (n = 8/group).
- (B) Frequencies of TAMs and CD8⁺ T cells from (A) (n = 7/group).
- (C) CyTOF UMAP plot of tumor-infiltrating T cells.
- (D) Subpopulations of CD8⁺ T cells and CD4⁺ T cells.
- (E) Median expressions of Ki67 and GZMB in CD8⁺ T cells.
- (F) Percentage of individual subclusters in CD8⁺ T cells.
- (G) Syngeneic KP2-OVA orthotopic model treated with vehicle or GB1275 for 12 days, and frequencies of GZMB⁺ CD8⁺ T cells (n = 7/group).
- (H) Gate of functional assay of CD8⁺ T cells from (G) (left). Percentage of functional CD8⁺ T cells (right) (n = 7/group). Graphs depict the mean ± SEM and * p < 0.05 using a two-sided t test for comparisons between two groups. Also see [Figure S2](#).



(legend on next page)

TCM amplified signaling differences. Importantly, STING protein expression was increased by GB1275 alone, and further increased when under TCM polarizing conditions (Figures 4B and S4B). We chose to focus on STING due to its known role in the induction of *Ifn* genes.

As expected for integrin activation, we observed increased phosphorylated FAK, PyK2, and SRC, and total myosin-IIa in BMDMs after 4 h GB1275 treatment (Figures 4C and S4C). In keeping with this, the GB1275 ability to induce *Ifnb1* and *Cxcl10* was lost when FAK was inhibited (Figure 4D). scRNA-seq analysis of TAMs *in vivo* also suggested that GB1275 activated oxidative phosphorylation and ROS pathways (Figures 3C, 3D, and 4E). In agreement with this, we observed increased HSP70 and SOD in BMDMs (Figure 4B).^{25,26} These data suggest that CD11b agonists might induce oxidative stress in TAMs. Evaluating this hypothesis *in vitro*, we found that GB1275 cooperated with TCM to enhance ROS production and this effect relied on FAK signaling (Figures 4F and S4D). To determine if ROS was critical for IFN gene induction, we pre-treated BMDMs with the ROS scavenger, N-acetylcysteine, and found loss of induction of *Ifnb1* and *Cxcl10* by GB1275 (Figure S4E). We next hypothesized that Sirtuin-3 (SIRT3) might link integrin-FAK signaling to ROS.²⁷ GB1275 suppressed SIRT3 in BMDMs, which was dependent on FAK (Figure 4G). Furthermore, GB1275 no longer induced ROS production or *Ifn* genes when SIRT3 was silenced (Figures 4H and S4G). These data suggest that integrin/FAK/SIRT3/ROS signaling is involved in the induction of IFN genes by CD11b agonists. However, the linkage to STING was unclear.

Previous studies have shown that high ROS could be linked to mitochondrial dysfunction and release of mitochondrial DNA (mtDNA), which could act as a primer for the cGAS-STING pathway.²⁸ Indeed, more mtDNA released into the cytosol following GB1275 treatment, which was amplified by TCM (Figure 4I). When depleting mtDNA by ethidium bromide²⁹ or DNase1, GB1275 induction of *Ifnb1* and *Cxcl10* was attenuated (Figures 4J, S4H, and S4I). Finally, analysis of TCM-polarized BMDMs showed that GB1275 increased expression of STING and phosphorylation of IRF3 and STAT1 (Figure 4K). When STING expression was lost by siRNA or using STING-null BMDMs, GB1275 was no longer able to increase *Ifn* gene

expression (Figures 4L, S4J, and S4K). Notably, GB1275 downregulated *If1* mRNAs independent of FAK activation, ROS, or STING expression (Figures S4L–S4N), suggesting two independent pathways under GB1275 regulation (Figure 4O). Together, CD11b agonists led to STING/IFN signaling in “tumor-primed” macrophages.

To determine the importance of STING in GB1275’s function *in vivo*, we transplanted mice with bone marrow (BM) from control or STING-null mice. After reconstitution, we implanted syngeneic KP2 tumors and found that GB1275’s effects on tumor progression and CD8⁺ T cells were dependent on STING activity in leukocytes (Figures 4M, 4N, and S4O). Together, these data suggest that CD11b agonists promote tumor immunity through myeloid STING activation.

In BM transplant studies, GB1275 reduced granulocytes independently of STING expression. However, decreases in TAMs were dependent on BM STING, suggesting that decreased TAM numbers by GB1275 may be linked to turnover following STING activation. Consistent with this possibility *in vitro*, prolonged exposure to high doses of GB1275 reduced cell number and phosphorylated AKT and increased cleaved caspase-3, partly dependent on STING expression (Figures S4P–S4S). This correlated with other studies showing STING/IFN signaling activation led to macrophage turnover.^{30,31}

The expression levels of STING in TAMs correlate with patient outcomes

Next, we analyzed STING/STAT1 activation by GB1275 in PDAC mouse models. In agreement with *in vitro* data, KPC tumors, as well as orthotopic KP2 and KI tumors had increased numbers of STING⁺ and pSTAT1⁺ total CD11b⁺ myeloid cells and TAMs (Figures 5A and S5A–S5C). Simultaneously, we observed a decrease in STING⁻ or pSTAT1⁻ np65⁺ TAMs by GB1275 (Figure 5A and S5A). These data demonstrate that GB1275 activates STING/STAT1 signaling *in vivo*.

Next, we studied the importance of STING expression in TAMs in human PDAC. Tissue microarrays from 173 surgical PDAC patients were stained by mIHC for CD8^α, STING, CD163, CD11b, and CK19 (Figure S5D). We defined macrophages as CD11b⁺, CD163⁺, and CK19⁻ and found that STING⁺ TAMs ranged from 1% to 60% of total TAMs, with an average of 16% of

Figure 3. GB1275 downregulates NF-κB/IL-1

- (A) UMAP scRNA-seq plots of the whole TAM/monocyte population (left), *Itgam* expression in this population (right).
- (B) UMAP scRNA-seq plots of subclusters from TAM/monocyte populations in 14 day vehicle- and GB1275-treated KP2 syngeneic model (left). Right, percentages of individual clusters.
- (C) GSEA-identified pathway enrichment in the whole TAM/monocyte population ($p < 0.05$).
- (D) GSEA-identified pathway enrichment in four subclusters ($p < 0.05$).
- (E) Volcano plot depicting GB1275-changed differentially expressed genes within the NF-κB/IL-1 signaling pathway from the whole TAM/monocyte population.
- (F) qPCR mRNA expression analysis of BMDMs treated with GB1275 for 7 h. Changes in gene expression are depicted as the fold change from the vehicle baseline.
- (G) Representative immunoblot for pp65, total p65, pIκB, total IκB, and β-actin (loading control) in BMDMs treated with GB1275 ± TCM for 7 h.
- (H) Representative immunoblot for total p65 and β-actin (loading control) in BMDMs treated with GB1275 for 7 h after 1 h MG132 pretreatment.
- (I) BMDMs were treated with GB1275 for 1 or 7 h after 1 h MG132 pretreatment. Immunoblot for p65 from total lysates and polymer-ubiquitin from purified p65 protein.
- (J–L) Representative mIHC staining for p65, CD11b, F4/80, and CK19 in tumors from 14 day vehicle- and GB1275-treated KPC mice (J), KP2 (K), and KI (L) orthotopic models. Scale bars, 100 μm. Right, percentage of np65⁺ TAMs ($n = 7$ –8 mice per group).
- (M) Kaplan-Meier survival curves for the top 80 downregulated NF-κB/IL-1 signaling-related genes from scRNA-seq (E) in TCGA patient dataset for pancreatic adenocarcinoma. Graphs show the mean ± SEM; * $p < 0.05$ using the two-sided t test for comparisons between two groups or log rank test for Kaplan-Meier survival curves. *In vitro* data are representative of three independent experiments. Also see Figure S3 and Tables S1, S2, and S3.

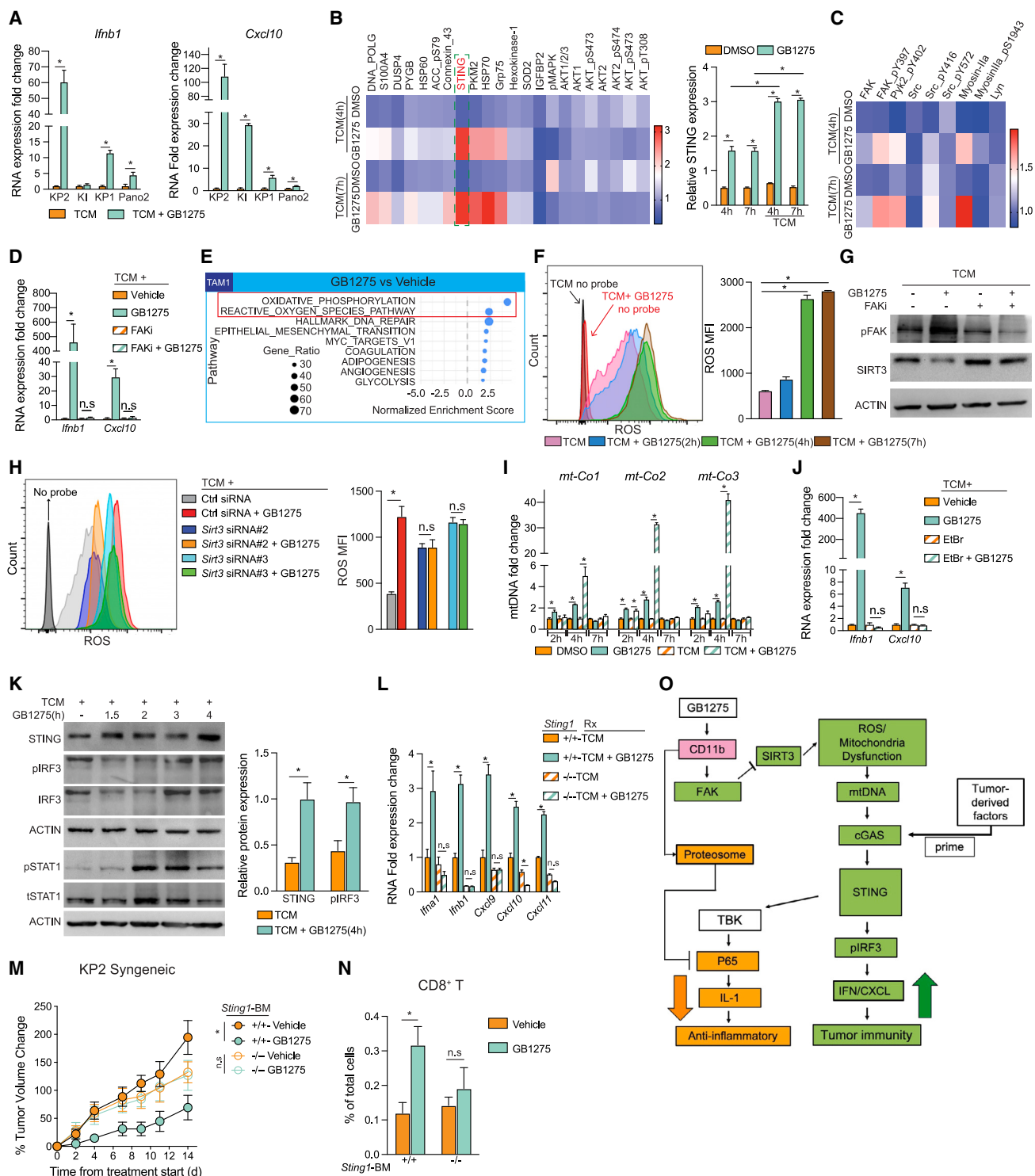


Figure 4. GB1275 increases IFN/CXCL transcription via STING

- (A) qPCR mRNA expression analysis of BMDMs treated with different TCM \pm GB1275 for 7 h. Changes in gene expression are depicted as the fold change from the vehicle baseline.
- (B) Heatmap of protein expression in BMDMs treated with vehicle or GB1275 \pm TCM for 4 and 7 h (left). Quantification of STING expression (right).
- (C) Heatmap of integrin signaling-related protein expression.
- (D) qPCR mRNA expression analysis of BMDMs treated with TCM \pm GB1275 for 7 h after 1 h FAKi pretreatment. Changes in gene expression are depicted as the fold change from the vehicle baseline.
- (E) GSEA-identified pathway enrichment in cluster TAM1 in 3B ($p < 0.05$).

(legend continued on next page)

TAMs expressing STING (Figures 5B and 5C). In PDAC tissues, higher percentages of STING⁺ TAMs or STING⁺CD11b⁺ cells correlated with increased CD8⁺ T cell infiltration (Figures 5D and S5E). Furthermore, high STING⁺ TAM infiltration correlated with longer survival (Figure 5E). Together, these data suggest that STING induction in TAMs might be indicative of better T cell responses and improved clinical outcomes.

Biomarker validation in the first-in-human GB1275 clinical trial

To determine if GB1275 could alter STING/STAT1 signaling in human tumors, we evaluated samples from a first-in-human clinical evaluation of the GB1275 (NTC04060342).³² The phase 1 portion of the study included a single-agent GB1275 dose escalation and safety evaluation either as monotherapy (regimen A) or in combination with pembrolizumab (regimen B). Both treatment regimens included patients with advanced treatment-refractory solid tumors. In these studies, GB1275 demonstrated good tolerability, even at the highest dose level.³² For a subset of patients, tumor tissues were available, and we performed mIHC for CD11b, CD163, pSTAT1, STING, p65, and pan-cytokeratin on 11 paired, pretreatment and post-treatment biopsy tissues (Figure 5F; Table S5). Compared with pretreatment tissues, GB1275 elevated the percentages of pSTAT1⁺ or STING⁺ TAMs in the majority of patients and across both regimens (Figures 5G, S5F, and S5G). As expected, we observed a correlation between STING and pSTAT1 expression in TAMs; and the percentage of STING⁺ TAMs correlated with increased CD8⁺ T cell infiltration (Figure 5H). The p65 expression in TAMs only decreased in 6 out of 11 patients, and the majority was observed in GB1275 single agent (4/6 in regimen A, 2/5 in regimen B, Figure S5G). This may not be surprising, as STING/STAT1 activation *in vivo* may overcome CD11b agonist's impact on NF-κB.^{33,34} Taken together, CD11b agonists increase STING/STAT1 activation in TAMs in advanced metastatic cancers.

DNA-damaging therapies cooperate with CD11b agonism to amplify IFN signaling

The above data demonstrated that CD11b agonists could activate STING/IFN signaling in TAMs. However, tumor parameters that might define the magnitude of this activation remained unclear. Notably, *in vitro*, GB1275 maximal induction of STING/

IFN signaling in macrophages was dependent on TCM (Figure 4A). Thus, we hypothesized that understanding what factors in TCM augmented STING activation might yield insight into how to further amplify this pathway. To accomplish this aim, we separated TCM into proteins >3 kDa, and small-molecule metabolites <3 kDa (Figure 6A). Next, we assayed whether TCM-derived proteins or small molecules synergized with GB1275. Notably, the TCM fraction containing metabolites and not proteins enhanced the induction of *Ifn* genes by GB1275 (Figure 6A). We hypothesized that the small molecules amplifying STING activation might be either whole-genomic DNA (gDNA) or mtDNA released by stressed or dying tumor cells in culture. To test this, we analyzed mtDNA and gDNA in TCM from standard culture or when treated with gemcitabine (GEM) (Figure S6A). Under untreated conditions, we could readily detect mtDNA but not gDNA in PDAC cell TCM (Figure S6B). However, both mtDNA and gDNA release was observed in GEM treatment PDAC cell TCM (Figure S6B). Moreover, TCM from PDAC cells treated with either GEM (GEM-TCM) or radiation therapy (RT) synergized with GB1275 to induce *Ifnb1* and *Cxcl10* expression in macrophages (Figures 6B and S6A). Moreover, when depleting DNA in the GEM-TCM with DNase1, GB1275 could no longer increase *Ifnb1* or *Cxcl10* expression (Figure S6C). These data suggest that even low levels of DNA released from stressed or dying tumor cells augments STING signaling activation by GB1275. Because GEM-treated PDAC cells release more DNA, we determined whether cell-damaging reagents synergized with GB1275 *in vivo*.

To determine if chemotherapy plus CD11b agonist could amplify IFN *in vivo*, we treated PDAC-bearing mice with GEM plus paclitaxel (GEM/PTX) (Figure 6C). As expected, GEM/PTX only modestly delayed tumor progression; however, when GEM/PTX was combined with GB1275, we observed reduced tumor burden and improved survival (Figure 6C). In parallel with significant increases in *Ifn* genes and increased IFN-β, CXCL10, and CXCL11 protein in combination-treated PDAC tissues (Figures 6D and 6E). To understand how this combination might impact chemotherapy-induced T cell priming, we analyzed tumor antigen-specific CD8⁺ T cells in orthotopic KP2-OVA-bearing mice. As expected, GB1275 increased the number of total CD8⁺ T cells as well as OVA-dextramer⁺ CTLs in PDAC tissues (Figure 6F), which were further improved in

(F) Intracellular total ROS in BMDMs stimulated by TCM + GB1275 for different time points (left). Quantification of ROS production (right).

(G) BMDMs were treated by TCM ± GB1275 for 4 h after 1 h FAK1 pretreatment. Representative immunoblots for pFAK, SIRT3, and β-actin (loading control).

(H) Intracellular total ROS in BMDMs transfected with *Sirt3* siRNA or ctrl siRNA for 24 h prior to 7 h TCM ± GB1275 (left). Quantification of ROS production (right).

(I) qPCR analysis of mitochondrial genes released in cytoplasm from BMDMs treated with vehicle or GB1275 ± TCM for the indicated time periods. Changes in gene expression are depicted as the fold change from the vehicle baseline.

(J) qPCR mRNA expression analysis of BMDMs treated with TCM ± GB1275 for 7 h after 1 h ethidium bromide (EtBr) pretreatment. Changes in gene expression are depicted as the fold change from the vehicle baseline.

(K) Representative immunoblots for STING, total IRF3, pIRF3, pSTAT1, total STAT1, and β-actin (loading control) in BMDMs treated with TCM ± GB1275 for the indicated time periods (left). Quantification of STING and pIRF3 relative expression (right).

(L) qPCR mRNA expression analysis of BMDMs isolated from wild-type or STING-null mice treated with TCM ± GB1275 for 7 h. Changes in gene expression are depicted as the fold change from the vehicle baseline.

(M) C57/BL-6 mice were lethally irradiated and adoptively transferred with BM from either wild-type mice or STING-null mice. KP2-syngeneic tumors were established on above mice and treated with vehicle or GB1275 for 14 days. Right, tumor growth curve expressed as percentages of tumor volume changes ($n = 7\text{--}8/\text{group}$).

(N) Tumor-infiltrate CD8⁺ T cell frequencies from the above mice ($n = 5\text{--}6/\text{group}$).

(O) The proposed model: GB1275 regulated two separate signaling pathways in macrophages, including p65/IL-1 inhibition and STING/IFN/CXCL axis activation. Graphs show the mean ± SEM; * $p < 0.05$ using the two-sided t test between two groups. *In vitro* data are representative of three independent experiments. Also see Figure S4 and Table S4.

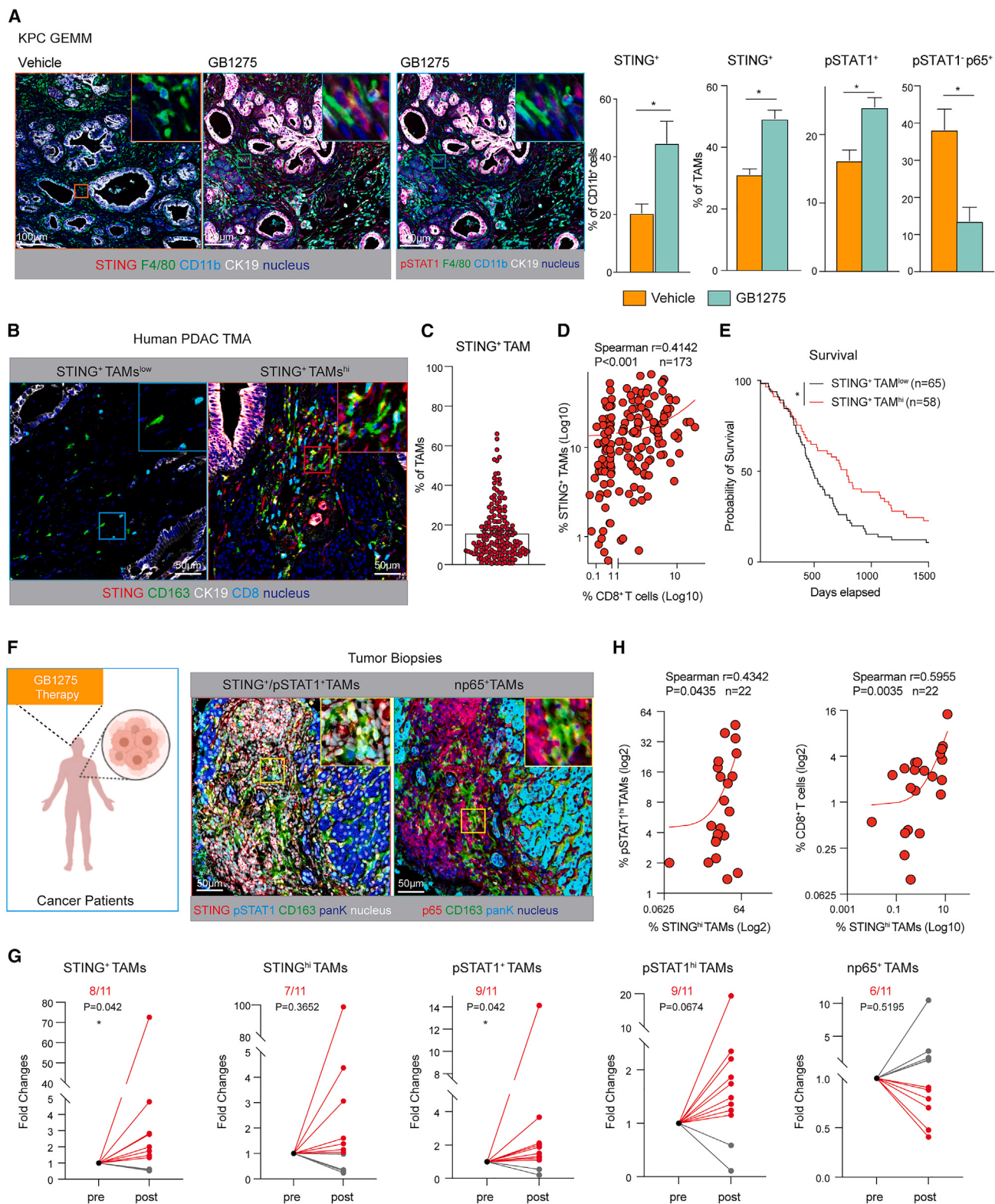


Figure 5. STING activation by GB1275 in mouse models and tumor biopsies

(A) Representative mIHC staining for pSTAT1, STING, F4/80, CD11b, and CK19 in tumors from 14 day vehicle- and GB1275-treated KPC mice. Scale bar, 100 μ m. Right, percentages of STING⁺ CD11b⁺ cells, STING⁺ TAMs, pSTAT1⁺ TAMs, and pSTAT1⁻ p65⁺ TAMs ($n = 7-9$ mice per group).

(B) Representative mIHC staining for STING, CD163, CK19, and CD8 α in human PDAC tissue microarrays (TMAs). Scale bars, 50 μ m.

(legend continued on next page)

combination with chemotherapy (Figures 6F and S6D). Interestingly, only in the combination-treated tumors did we see increased proliferation in OVA-specific CTLs (Figure 6F). Analysis of tumor-draining lymph nodes (dLNs) showed that GB1275 enhanced the ability of GEM/PTX to increase/prime tumor-specific CD8⁺ T cells (Figures 6G and S6E). To determine if priming of T cells by the combination required STING signaling in leukocytes, we transplanted mice with WT or STING-null BM. In these mice, in both tumor tissues and dLNs, adding GB1275 to GEM/PTX doubled the number and proliferation of tumor-specific CD8⁺ T cells, which were dependent on STING in BM-derived cells (Figures 6H, 6I, S6F, and S6G). In contrast, chemotherapy-induced tumor-specific CTLs were not impacted by loss of STING in the BM (Figures 6H and 6I). Together, GB1275 synergizes with chemotherapy to prime T cell responses.

Innate agonists synergize with CD11b-agonists

To determine what other strategies could synergize with CD11b agonism, we treated macrophages with GB1275 and sub-saturating doses of TLR7, TLR9, or STING agonists, and compared this with the combination with TCM from GEM-treated PDAC cells. In each condition, GB1275 synergized to dramatically increase *Ifn* gene expression, with some combinations increasing *Ifn* genes by over >100-fold (Figure 7A). As expected, TCMs with TLR7-, TLR9-, and STING-agonists all also increased *Il1a*, *Il1b*, and *Cd274* expression (Figure 7B), likely through NF-κB activation. However, GB1275 given in combination suppressed these inflammatory genes (Figure 7B). Single-agent GB1275 also led to extracellular recycling of TLR9 protein, which was required for *Cxcl9*, *10*, and *11* gene inductions in GB1275 plus GEM-TCM combinations (Figures S7A and S7B), possibly indicating the importance of TLR9 in DNA sensing during chemotherapy combinations. Together, the CD11b agonist synergizes with an innate immune agonist to drive IFNs in macrophages.

We next determined if GB1275 improved the efficacy of innate agonists *in vivo*. KPC GEMMs and syngeneic tumor-bearing mice were treated with vehicle or GB1275 ± TLR agonists. While both the TLR7 and TLR9 agonists inhibited tumor progression, the combination with GB1275 was superior in syngeneic PDAC models (Figure 7C). In KPC GEMMs, adding GB1275 to the TLR9 agonist decreased tumor burden and increased CD8⁺ CTL infiltration (Figures 7D and S7C). We next determined the efficiency of GB1275 combined with the STING agonist. PDAC-bearing mice were treated with intratumoral injection of the STING agonist, ADU-S100 ± GB1275. Both GB1275 and ADU-S100 suppressed tumor progression, but the combination was superior (Figure 7E). Similarly, both GB1275 and ADU-S100 both increased CD8⁺ T cell infiltration, but the highest levels were seen in the combination in both syngeneic models and

GEMMs (Figures 7F and 7G). Both STING agonists and GB1275 reduced TAM numbers (Figure 7E), possibly due to macrophage turnover. Finally, the tumor control of STING agonist alone was not affected by T cell depletion; however, combination was dependent on T cells (Figure 7G). These data suggest that CD11b agonists and innate immune agonists work synergistically *in vivo*.

We next studied the immune changes induced by the combination of GB1275 and STING activation. UMAP analysis of T cell CyTOF data identified several populations of CD8⁺ and CD4⁺ T cells (Figures 7H and S7D). Compared with single agents, the combination markedly shifted CD8⁺ T cells toward proliferative effector T-bet^{hi}/GZMB^{hi}/Ki67^{hi} phenotype (cluster 2) at the expense of memory (cluster 1) and non-proliferative subsets (cluster 3) (Figures 7I and S7E). The combination also significantly increased GZMB expression across CD8⁺ T cells (Figure 7J). Interestingly, CTLA-4, not PD-1, expression was enhanced in combination (Figures 7J and S7E). Similar to single-agent GB1275, the impact on CD4⁺ T cells was modest. The combination increased activated CD4⁺ Th cells expressing low PD-1 (cluster 4) and decreased Tregs expressing high PD-1 (cluster 2) (Figures S7F–S7I). Together, in addition to T cell numbers, CD11b agonists and STING agonists synergize to enhance effector CD8⁺ CTLs.

We next analyzed myeloid cells. UMAP analysis identified clusters of TAMs, monocytes, and granulocytes (Figure 7K). In TAMs, the combination of GB1275 and ADU-S100 decreased Sirpx^{high} (cluster 4) and Ki67⁺ MHC-II^{low} TAMs (cluster 5), but markedly increased TAMs expressing high levels of CD80, CD86, MHC-II, and MHC-I (cluster 6) (Figures 7K and S7J), suggesting a shift from phagocytotic and proliferative TAMs toward antigen presentation. In addition, PD-L1 expression among TAMs, granulocytes, and conventional dendritic cells (cDCs) (Figures S7K–S7N) was increased. To verify whether STING signaling activation improved the efficacy of GB1275 in PDAC, we treated PDAC-bearing mice with GB1275 + RT ± STING agonist and observed that the combination regressed tumors and improved survival (Figure 7L). These data suggest that GB1275 renders the STING agonist more effective at inducing anti-tumor immunity.

DISCUSSION

PDAC is known to be poorly responsive to immunotherapy.³⁵ We assessed a cross-tumor comparison of TAM phenotypes by scRNA-seq and found that TAMs in PDAC had lower IFN and antigen presentation signatures. In keeping with this assessment, in PDAC and CRC biopsy tissues we observed minimal percentages of STING⁺ or pSTAT1⁺ TAMs, suggesting weaker IFN

(C) Average percentage of STING⁺ TAMs from the TMAs.

(D) Scatterplot showing Spearman's correlation between the percentage of STING⁺ macrophages and CD8⁺ T cells from (B).

(E) Kaplan-Meier survival curves for patients with high STING⁺ TAM infiltration and low STING⁺ TAM infiltration from (B).

(F) Representative mIHC staining for STING, pSTAT1, p65, CD163, and pan-keratin (PanK) in 11 paired tumor biopsies from patients. Scale bars, 50 μm.

(G) Relative fold changes of STING⁺, STING^{hi} macrophages, pSTAT1⁺, pSTAT1^{hi} macrophages, and nuclear p65⁺ macrophages in paired pre- and post-groups.

(H) Scatterplots showing Spearman's correlations between the percentage of STING^{hi} macrophages and pSTAT1^{hi} macrophages in all 22 tumor biopsies.

Scatterplots showing Spearman's correlation between the percentages of STING^{hi} macrophages (out of total cells) and CD8⁺ T cells in all 22 tumor biopsies (right). Graphs show the mean ± SEM; *p < 0.05 using the two-sided t test between two groups, one sample t test, and Wilcoxon tests, or the log rank test for Kaplan-Meier survival curves. Also see Figure S5 and Table S5.

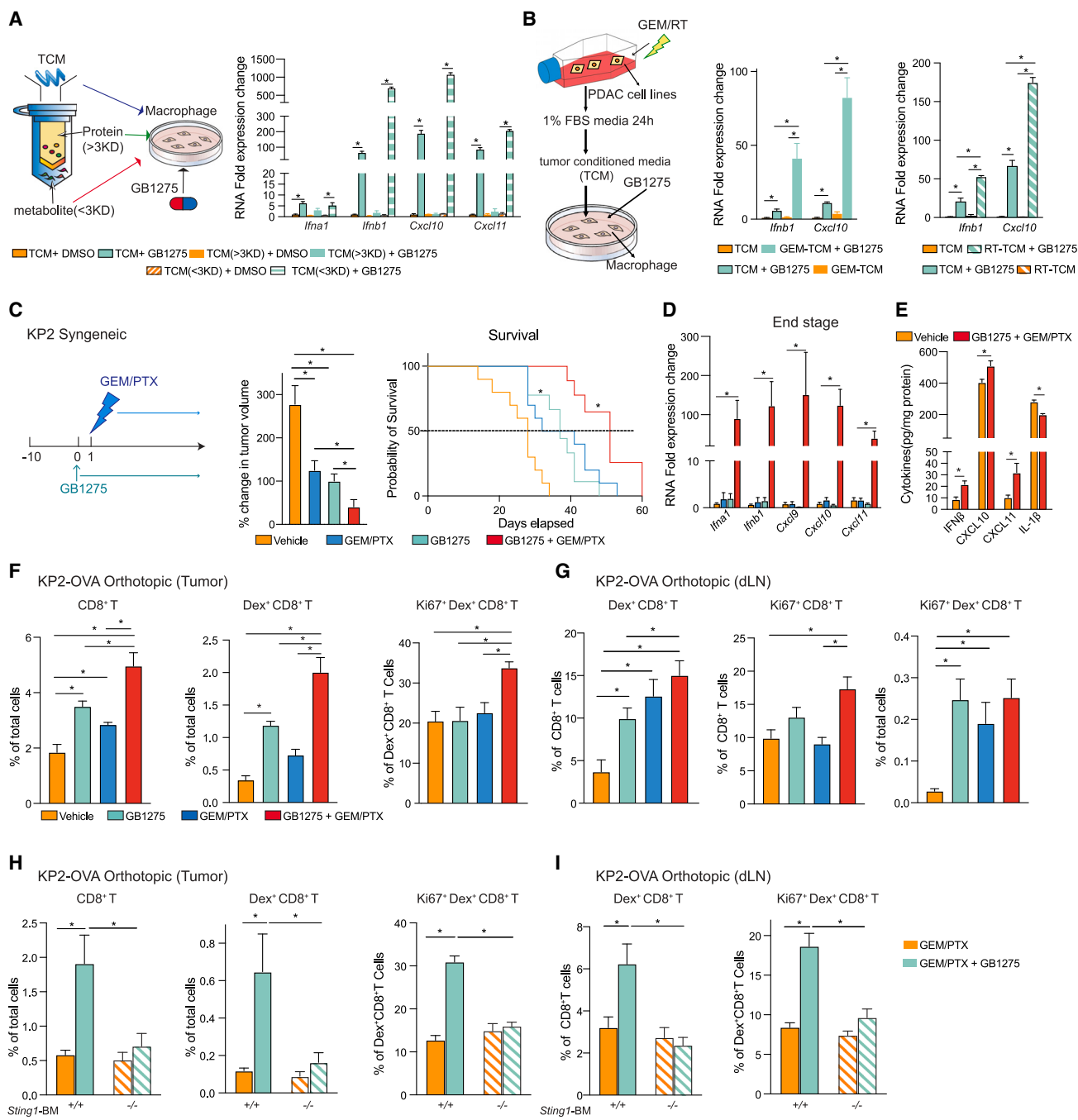


Figure 6. Chemotherapy or radiation therapy combined with GB1275 amplifies STING/IFN signaling

(A) Concentrated protein (>3 kDa) and metabolites (<3 kDa) in TCM were separated by a protein concentrator (left). qPCR mRNA expression analysis of BMDMs treated with different fractions of TCM ± GB1275 for 7 h. Changes in gene expression are depicted as the fold change from the vehicle baseline (right).

(B) KP2 cells were treated with either gemcitabine (left) or radiation (right). TCM was made from the above cells. qPCR mRNA expression analysis of BMDMs treated with the above-mentioned TCM ± GB1275 for 7 h. Changes in gene expression are depicted as the fold changes from the vehicle baseline.

(C) Tumor growth of KP2 syngeneic model treated with vehicle or GB1275 ± chemotherapy (left). Mean percent change in tumor volume on day 12 (n = 9–10/group) (middle). Right, Kaplan-Meier survival analysis (n = 9–10/group).

(D) qPCR mRNA expression analysis of tissue from (C) (n = 6–8/group). Changes in gene expression are depicted as fold changes from the vehicle baseline.

(E) IFN- β , CXCL10, 11, and IL-1 β production in tissues from a syngeneic KP2-OVA orthotopic model treated with vehicle or GB1275 + chemotherapy for 12 days (n = 7–8 group).

(F) Syngeneic KP2-OVA orthotopic model treated with vehicle, GB1275, chemotherapy, or combination for 12 days. Frequencies of tumor-infiltrating CD8+ T cells, Dex+ CD8+ T cells, and proliferative Dex+ CD8+ T cells (n = 6/group).

(G) Frequencies of Dex+ CD8+ T cells, proliferative CD8+ T cells, and proliferative Dex+ CD8+ T cells in tumor-draining lymph nodes (dLNs) from (F).

(legend continued on next page)

signaling in TAMs in these cancers. In contrast, IL-1 and tissue remodeling signatures were higher in PDAC, consistent with the stromal desmoplastic response characteristic of this tumor type. Hence, we postulate inducing IFN signaling in myeloid cells to rescue tumor immunity in some tumor types.

The cGAS-STING signaling pathway has been regarded as important DNA sensing machinery, allowing immune responses to infections, inflammation, and cancer.³⁶ However, activated STING plays a complicated role in cancer.³⁷ On one hand, STING activation induces anti-tumor responses via increased interferon secretion and lymphocyte infiltration, which is promising for cancer immunotherapy.³⁸ STING downregulation could be a factor driving resistance to immune effectors in cancer models,³⁹ and STING signaling activation increases intratumoral T cell number consistent with upregulated IFN signatures.⁴⁰ Improved productive T cell priming via cDC1s occurs in STING activation conditions.⁴¹ These experiments validate that STING/IFN signaling activation has anti-tumorigenic properties. On the other hand, emerging evidence indicated the pro-tumoral role of the cGAS-STING pathway in some cancer models.^{42,43} STING activation-dependent inflammation could be the major factor driving tumor development.⁴⁴ STING activation results in TANK-binding kinase-1/NF-κB-dependent inflammatory cytokine production,^{45,46} supporting cancer cell growth and chemo-resistance.⁴⁷ Blood vessel disruption was observed after STING agonist, owing to TNF- α secretion.⁴⁸ The anti-tumoral role of STING activation could be characterized as enhanced IFN production, while the side effects might be from p65-mediated inflammatory cytokine release. In our study, CD11b-agonists regulated two separate signaling pathways, including STING/IFN and p65 inhibition. The latter may decrease side effects of STING activation.

In our PDAC models, blocking p65/IL-1R signaling impacted myeloid cell infiltration and tumor progression, but did not regulate T cell infiltration, possibly suggesting that IFN induction is needed to improve T cell infiltration and/or function. NF-κB/IL-1 signature downregulation was related to clinical outcomes of PDAC patients in TCGA; however, the role of NF-κB in PDAC is still controversial. NF-κB and autophagy signaling activation could reprogram the M2-like phenotype to the M1 phenotype.^{49,50} TNF- α signaling-mediated apoptosis of CD206⁺ TAMs led to augmented anti-tumor immunity.⁵¹ Moreover, non-canonical NF-κB signaling activation by cIAP1/2 antagonists stimulated the T cell-TAM axis to inhibit tumor progression. CD40 activation in TAMs infiltrated into tumor tissue, reprogramming tumor stroma,⁵² and p65 was involved in CD40 activation-induced proinflammatory gene expression.⁵³ On the other hand, NF-κB acts as a key link between inflammation and PDAC. Chronic inflammatory cytokine secretions, such as IL-1 and IL-6, regulated by p65, led to tumor progression.⁵⁴ p65 activation-mediated CXCL14 promoted angiogenesis and tumor growth,⁵⁵ and p65 could regulate HIF1- α and VEGF α to affect epithelial-mesenchymal transition and angiogenesis.⁵⁶ NF-κB

inhibition has shown great potential to inhibit PDAC; however, precise regulation of p65 in PDAC is still not well understood.

Previous studies have demonstrated efficacy of GB1275, a CD11b agonist, in preclinical models,^{17–19,57} and our data identified that GB1275 reprogramed solid tumor immunity through activation of STING-IFN signaling in TAMs. GB1275 entered clinical investigation (NCT04060342), and analyses of STING/pSTAT1 and p65 expression in a limited number of pre- and post-treatment patient tissues are consistent with GB1275 target engagement at the tumor site and suggest the translatability of our mechanistic findings. Specifically, aligned with PDAC model data, GB1275 increased the presence of STING⁺ and pSTAT1⁺ TAMs in post-treatment biopsies in the majority of samples tested. In parallel, a reduction in p65⁺ TAMs in post-treatment biopsies was observed in a subset of treated patients. Pharmacodynamic response heterogeneity may be attributable to differential TAM phenotypes/functional states across the different indications studied, as highlighted by our scRNA-seq analysis of TAMs across different cancers. Alternatively, the observed heterogeneity may be highlighting differences in the TME (e.g., the presence of mtDNA), as GB1275-mediated STING activation is context dependent. Early clinical studies with GB1275 have shown limited efficacy to date.⁵⁷ Our data on the GB1275 mechanism of action suggests that the anti-tumor response of CD11b agonists could enhance DNA damage-inducing agents, and that future clinical exploration may be warranted.

STAR★METHODS

Detailed methods are provided in the online version of this paper and include the following:

- KEY RESOURCES TABLE
- RESOURCE AVAILABILITY
 - Lead contact
 - Materials availability
 - Data and code availability
- EXPERIMENTAL MODEL AND SUBJECT DETAILS
 - Human tumor tissue
 - The genetic mouse PDAC model and other mouse models
 - Cell lines, pharmacologic compounds and *in vivo* antibodies
 - Syngeneic model and preclinical animal cohorts
- METHOD DETAILS
 - Tissue harvesting
 - Mass cytometry (CyTOF)
 - Single-cell RNA sequencing data analysis in humans
 - Single-cell RNA sequencing data analysis in mice
 - Mouse tissue isolation and flow cytometry
 - Immunohistochemistry and mIHC
 - Macrophage depletion

(H) C57/BL-6 mice were lethally irradiated and adoptively transferred with BM from either wild-type mice or STING-null mice. KP2-OVA orthotopic model was established on the above mice and treated with chemotherapy ± GB1275 for 12 days. Frequencies of tumor-infiltrating CD8⁺ T cells, Dex⁺ CD8⁺ T cells, and proliferative Dex⁺ CD8⁺ T cells (n = 6/group).

(I) Frequencies of Dex⁺ CD8⁺ T cells and proliferative Dex⁺ CD8⁺ T cells in dLN from (H). The graphs show mean ± SEM; *p < 0.05 using the two-sided t test between two groups or log rank test for Kaplan-Meier survival curves. *In vitro* data are representative of three independent experiments. Also see Figure S6.

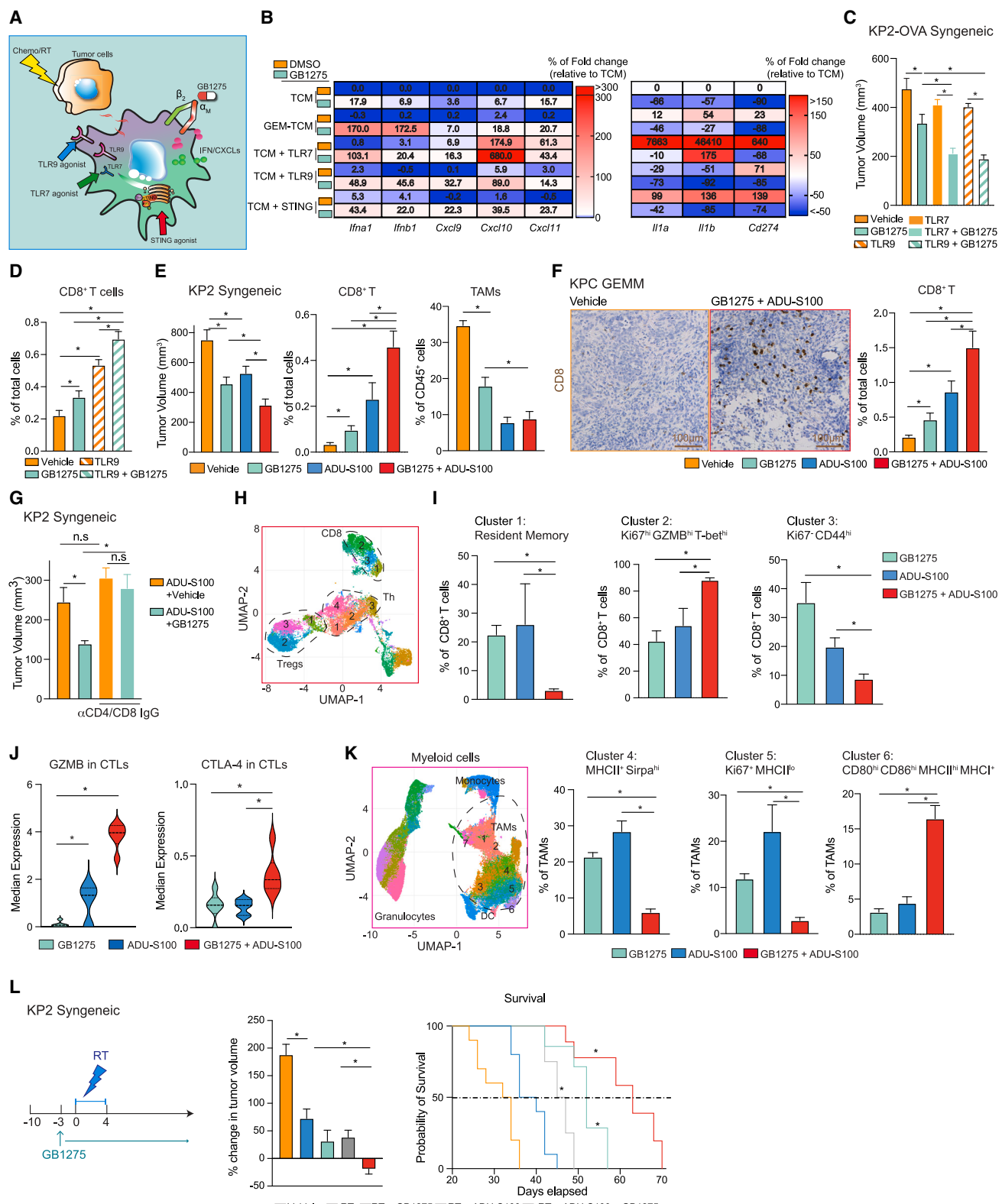


Figure 7. STING agonist synergizes with GB1275 and remodels TME

(A) Schematic of several combinations of GB1275.

(B) Heatmap of relative mRNA expression from BMDMs after treatment (A). Percentages of changes in gene expression are depicted as the fold change from the vehicle baseline.

(legend continued on next page)

- Small animal radiation therapy (RT)
- Bone marrow transplantation
- Isolation of bone marrow-derived macrophages
- RNA isolation and real-time PCR
- Reverse-phase protein array (RPPA)
- Cytokine assay
- Western immunoblot and immunoprecipitation (IP)
- Isolate released mtDNA
- Measuring ROS production
- Cell proliferation assay
- *In vitro* siRNA treatment
- Isolation of human CD14⁺ monocyte-derived macrophages
- Separation of TCM
- **QUANTIFICATION AND STATISTICAL ANALYSIS**
 - Statistical analyses

SUPPLEMENTAL INFORMATION

Supplemental information can be found online at <https://doi.org/10.1016/j.ccel.2023.04.018>.

ACKNOWLEDGMENTS

D.G.D. was supported by NCI R01CA273190 R01CA177670, R01CA203890, P30CA09184215, P50CA196510, and WUSM CCSG grants and the BJC Cancer Frontier Fund. J.K.S. was supported by S100D020136-01. The authors would like to thank Gossamer Bio for providing reagents and clinical samples.

AUTHOR CONTRIBUTIONS

Conceptualization. X.L. and D.G.D.; methodology, X.L., C.M., J.K.S., V.G., and D.G.D.; investigation, X.L., G.D.H., N.C.B., B.L.K., J.-M.B., C.Z., V.E.L., C.M., F.A., and L.-I.K.; writing – original draft, X.L., D.G.D., R.E.O., A.V.G., L.L.C., and V.G.; writing – review & editing, X.L. and D.G.D.; funding, D.G.D.; resources, H.P., R.E.O., A.V.G., J.-M.B., K.R.V., L.L.C., R.C.F., and D.G.D.; supervision, D.G.D.

DECLARATION OF INTERESTS

D.G.D. is on the scientific advisory board for Adhaere, 149.Bio, and Gossamer Bio. R.E.O., A.V.G., J.-M.B., and L.L.C. are employees from Gossamer Bio.

INCLUSION AND DIVERSITY

We support inclusive, diverse, and equitable conduct of research.

Received: May 26, 2022
Revised: April 14, 2023
Accepted: April 27, 2023
Published: May 25, 2023

REFERENCES

1. DeNardo, D.G., and Ruffell, B. (2019). Macrophages as regulators of tumour immunity and immunotherapy. *Nat. Rev. Immunol.* 19, 369–382. <https://doi.org/10.1038/s41577-019-0127-6>.
2. Biswas, S.K., and Mantovani, A. (2010). Macrophage plasticity and interaction with lymphocyte subsets: cancer as a paradigm. *Nat. Immunol.* 11, 889–896. <https://doi.org/10.1038/ni.1937>.
3. Erkan, M., Hausmann, S., Michalski, C.W., Fingerle, A.A., Dobritz, M., Kleeff, J., and Friess, H. (2012). The role of stroma in pancreatic cancer: diagnostic and therapeutic implications. *Nat. Rev. Gastroenterol. Hepatol.* 9, 454–467. <https://doi.org/10.1038/nrgastro.2012.115>.
4. Ruffell, B., and Coussens, L.M. (2015). Macrophages and therapeutic resistance in cancer. *Cancer Cell* 27, 462–472. <https://doi.org/10.1016/j.ccr.2015.02.015>.
5. Schmid, M.C., and Varner, J.A. (2012). Myeloid cells in tumor inflammation. *Vasc. Cell* 4, 14. <https://doi.org/10.1186/2045-824X-4-14>.
6. Hu, H., Jiao, F., Han, T., and Wang, L.W. (2015). Functional significance of macrophages in pancreatic cancer biology. *Tumour Biol.* 36, 9119–9126. <https://doi.org/10.1007/s13277-015-4127-2>.
7. Lecoultrre, M., Dutoit, V., and Walker, P.R. (2020). Phagocytic function of tumor-associated macrophages as a key determinant of tumor progression control: a review. *J. Immunother. Cancer* 8, e001408. <https://doi.org/10.1136/jitc-2020-001408>.
8. Martinez, F.O., Gordon, S., Locati, M., and Mantovani, A. (2006). Transcriptional profiling of the human monocyte-to-macrophage differentiation and polarization: new molecules and patterns of gene expression. *J. Immunol.* 177, 7303–7311. <https://doi.org/10.4049/jimmunol.177.10.7303>.
9. Gordon, S., and Taylor, P.R. (2005). Monocyte and macrophage heterogeneity. *Nat. Rev. Immunol.* 5, 953–964. <https://doi.org/10.1038/nri1733>.
10. Gordon, S., and Martinez, F.O. (2010). Alternative activation of macrophages: mechanism and functions. *Immunity* 32, 593–604. <https://doi.org/10.1016/j.immuni.2010.05.007>.
11. Kurahara, H., Shinchi, H., Mataki, Y., Maemura, K., Noma, H., Kubo, F., Sakoda, M., Ueno, S., Natsugoe, S., and Takao, S. (2011). Significance of M2-polarized tumor-associated macrophage in pancreatic cancer. *J. Surg. Res.* 167, e211–e219. <https://doi.org/10.1016/j.jss.2009.05.026>.
12. Yoshikawa, K., Mitsunaga, S., Kinoshita, T., Konishi, M., Takahashi, S., Gotohda, N., Kato, Y., Aizawa, M., and Ochiai, A. (2012). Impact of tumor-associated macrophages on invasive ductal carcinoma of the

- (C) Tumor burden from the KP2-OVA syngeneic mouse model treated with vehicle or GB1275 ± TLR7 agonist or TLR9 agonist for 14 days ($n = 9\text{--}10/\text{group}$).
(D) Immunohistochemical staining for CD8⁺ T cells in tumors from 14 day vehicle, GB1275, TLR9 agonist, or combination-treated KPC mice. Right, average percentage of CD8⁺ T.
(E) Tumor burden from the KP2 syngeneic mouse model treated with vehicle or GB1275 ± ADU-S100 for 19 days ($n = 10/\text{group}$). Frequencies of tumor-infiltrating CD8⁺ T cells and macrophages ($n = 6/\text{group}$).
(F) Immunohistochemical staining for CD8⁺ T cells in tumors from 14 day vehicle-, GB1275-, ADU-S100-, or combination-treated KPC mice. Scale bars, 100 μm . Right, average percentage of CD8⁺ T cells ($n = 6\text{--}7/\text{group}$).
(G) Tumor burden from KP2 syngeneic mouse model treated with ADU-S100 or combination of GB1275 ± CD4/CD8⁺ T cell depletion for 12 days (left).
(H) KP2 syngeneic model treated with GB1275, ADU-S100, or combination for 14 days (left). CyTOF UMAP plot of tumor-infiltrating T cells, including CD8⁺ T cells, Th, and Tregs ($n = 6/\text{group}$).
(I) Percentages of individual subclusters in CD8⁺ T cells.
(J) Median expressions of GZMB and CTLA-4 in CD8⁺ T cells.
(K) CyTOF UMAP plot of tumor-infiltrating myeloid cells, including TAMs, granulocytes, monocytes, and dendritic cells from (H) ($n = 6/\text{group}$) (left). Percentages of individual subclusters in TAMs (right).
(L) Tumor growth of KP2 syngeneic model treated with vehicle or GB1275 ± radiation therapy (6 Gy \times 5) ± ADU-S100 (middle). (Right) Kaplan-Meier survival analyses ($n = 10/\text{group}$). Graphs show the mean \pm SEM; * $p < 0.05$ using the two-sided t test between two groups, analysis of variance or log rank test for Kaplan-Meier survival curves. *In vitro* data are representative of three independent experiments. Also see Figure S7.

- pancreas head. *Cancer Sci.* 103, 2012–2020. <https://doi.org/10.1111/j.1349-7006.2012.02411.x>.
13. Zhu, Y., Hawkins, W.G., and DeNardo, D.G. (2015). Reprogramming myeloid responses to improve cancer immunotherapy. *Oncolmmunology* 4, e974399. <https://doi.org/10.4161/2162402X.2014.974399>.
14. Nywening, T.M., Belt, B.A., Cullinan, D.R., Panni, R.Z., Han, B.J., Sanford, D.E., Jacobs, R., Ye, J., Patel, A.A., et al. (2018). Targeting both tumour-associated CXCR2(+) neutrophils and CCR2(+) macrophages disrupts myeloid recruitment and improves chemotherapeutic responses in pancreatic ductal adenocarcinoma. *Gut* 67, 1112–1123. <https://doi.org/10.1136/gutjnl-2017-313738>.
15. Mitchem, J.B., Brennan, D.J., Knolhoff, B.L., Belt, B.A., Zhu, Y., Sanford, D.E., Belaygorod, L., Carpenter, D., Collins, L., Piwnica-Worms, D., et al. (2013). Targeting tumor-infiltrating macrophages decreases tumor-initiating cells, relieves immunosuppression, and improves chemotherapeutic responses. *Cancer Res.* 73, 1128–1141. <https://doi.org/10.1158/0008-5472.CAN-12-2731>.
16. Stromnes, I.M., Brockenbrough, J.S., Izeradjene, K., Carlson, M.A., Cuevas, C., Simmons, R.M., Greenberg, P.D., and Hingorani, S.R. (2014). Targeted depletion of an MDSC subset unmasks pancreatic ductal adenocarcinoma to adaptive immunity. *Gut* 63, 1769–1781. <https://doi.org/10.1136/gutjnl-2013-306271>.
17. Schmid, M.C., Khan, S.Q., Kaneda, M.M., Pathria, P., Shepard, R., Louis, T.L., Anand, S., Woo, G., Leem, C., Faridi, M.H., et al. (2018). Integrin CD11b activation drives anti-tumor innate immunity. *Nat. Commun.* 9, 5379. <https://doi.org/10.1038/s41467-018-07387-4>.
18. Panni, R.Z., Herndon, J.M., Zuo, C., Hegde, S., Hogg, G.D., Knolhoff, B.L., Breden, M.A., Li, X., Krisnawan, V.E., Khan, S.Q., et al. (2019). Agonism of CD11b reprograms innate immunity to sensitize pancreatic cancer to immunotherapies. *Sci. Transl. Med.* 11, eaau9240. <https://doi.org/10.1126/scitranslmed.aau9240>.
19. Zhao, Q., Lu, L., Du, G., Wang, Z., Li, X., and Ju, F. (2020). 15-hydroxy-6 alpha,12-epoxy-7 beta,10 alpha H,11 beta H-spiroax-4-ene-12-one sensitizes rectal tumor cells to anti-PD1 treatment through agonism of CD11b. *Immunopharm Immunot* 42, 358–365. <https://doi.org/10.1080/08923973.2020.1778722>.
20. Zhu, Y., Herndon, J.M., Sojka, D.K., Kim, K.W., Knolhoff, B.L., Zuo, C., Cullinan, D.R., Luo, J., Bearden, A.R., Lavine, K.J., et al. (2017). Tissue-resident macrophages in pancreatic ductal adenocarcinoma originate from embryonic hematopoiesis and promote tumor progression. *Immunity* 47, 323–338.e6. <https://doi.org/10.1016/j.immuni.2017.07.014>.
21. Bloom, M.J., Saksena, S.D., Swain, G.P., Behar, M.S., Yankeelov, T.E., and Sorace, A.G. (2019). The effects of IKK-beta inhibition on early NF-kappa-B activation and transcription of downstream genes. *Cell. Signal.* 55, 17–25. <https://doi.org/10.1016/j.cellsig.2018.12.004>.
22. Davoodi, H., Hashemi, S.R., and Seow, H.F. (2012). Increased NFk-B activity in HCT116 colorectal cancer cell line harboring TLR4 Asp299Gly variant. *Iran. J. Allergy, Asthma Immunol.* 11, 121–132.
23. Hu, X., Zhang, H., Zhuang, L., Jin, G., Yang, Q., Li, M., Sun, W., and Chen, F. (2020). Ubiquitin-Fold modifier-1 participates in the diabetic inflammatory response by regulating NF-kappaB p65 nuclear translocation and the ubiquitination and degradation of IkappaBalph. *Drug Des. Devel. Ther.* 14, 795–810. <https://doi.org/10.2147/DDDT.S238695>.
24. Pereira, S.G., and Oakley, F. (2008). Nuclear factor-kappaB1: regulation and function. *Int. J. Biochem. Cell Biol.* 40, 1425–1430. <https://doi.org/10.1016/j.biocel.2007.05.004>.
25. Moriyama-Gonda, N., Igawa, M., Shiina, H., Urakami, S., Shigeno, K., and Terashima, M. (2002). Modulation of heat-induced cell death in PC-3 prostate cancer cells by the antioxidant inhibitor diethyldithiocarbamate. *BJU Int.* 90, 317–325. <https://doi.org/10.1046/j.1464-410x.2002.02810.x>.
26. Doganlar, O., and Doganlar, B. (2015). Responses of antioxidant enzymes and heat shock proteins in *Drosophila* to treatment with a pesticide mixture. *Arch. Biol. Sci.* 67, 869–876. <https://doi.org/10.2298/Abs141031046d>.
27. Dai, L., Xie, Y., Zhang, W., Zhong, X., Wang, M., Jiang, H., He, Z., Liu, X., Zeng, H., and Wang, H. (2021). Weighted gene Co-expression network analysis identifies ANGPTL4 as a key regulator in diabetic cardiomyopathy via FAK/SIRT3/ROS pathway in cardiomyocyte. *Front. Endocrinol.* 12, 705154. <https://doi.org/10.3389/fendo.2021.705154>.
28. Riley, J.S., Quarato, G., Cloix, C., Lopez, J., O'Prey, J., Pearson, M., Chapman, J., Sesaki, H., Carlin, L.M., Passos, J.F., et al. (2018). Mitochondrial inner membrane permeabilisation enables mtDNA release during apoptosis. *EMBO J.* 37, e99238. <https://doi.org/10.1525/embj.201899238>.
29. Yu, M., Shi, Y., Wei, X., Yang, Y., Zhou, Y., Hao, X., Zhang, N., and Niu, R. (2007). Depletion of mitochondrial DNA by ethidium bromide treatment inhibits the proliferation and tumorigenesis of T47D human breast cancer cells. *Toxicol. Lett.* 170, 83–93. <https://doi.org/10.1016/j.toxlet.2007.02.013>.
30. Klaas, L., Vier, J., Gentle, I.E., Hacker, G., and Kirschnek, S. (2021). Diversity of cell death signaling pathways in macrophages upon infection with modified vaccinia virus Ankara (MVA). *Cell Death Dis.* 12. <https://doi.org/10.1038/s41419-021-04286-3>.
31. Murthy, A.M.V., Robinson, N., and Kumar, S. (2020). Crosstalk between cGAS-STING signaling and cell death. *Cell Death Differ.* 27, 2989–3003. <https://doi.org/10.1038/s41418-020-00624-8>.
32. Park, H., Bendell, J.C., Messersmith, W.A., Rasco, D.W., De Bono, J.S., Strickler, J.H., Zhou, L., Carter, L.L., Bruey, J.-M., Li, J., et al. (2021). Preliminary clinical and biologic results of GB1275, a first-in-class oral CD11b modulator, alone and with pembrolizumab, in advanced solid tumors (KEYNOTE A36). *J. Clin. Oncol.* 39, 2505. https://doi.org/10.1200/JCO.2021.39.15_suppl.2505.
33. Balka, K.R., Louis, C., Saunders, T.L., Smith, A.M., Calleja, D.J., D'Silva, D.B., Moghaddas, F., Tailler, M., Lawlor, K.E., Zhan, Y., et al. (2020). TBK1 and IKKepsilon act redundantly to mediate STING-induced NF-kappaB responses in myeloid cells. *Cell Rep.* 31, 107492. <https://doi.org/10.1016/j.celrep.2020.03.056>.
34. Dunphy, G., Flannery, S.M., Almine, J.F., Connolly, D.J., Paulus, C., Jonsson, K.L., Jakobsen, M.R., Nevels, M.M., Bowie, A.G., and Unterholzner, L. (2018). Non-canonical activation of the DNA sensing adaptor STING by ATM and IFI16 mediates NF-kappaB signaling after nuclear DNA damage. *Mol. Cell* 71, 745–760.e5. <https://doi.org/10.1016/j.molcel.2018.07.034>.
35. Balachandran, V.P., Beatty, G.L., and Dougan, S.K. (2019). Broadening the impact of immunotherapy to pancreatic cancer: challenges and opportunities. *Gastroenterology* 156, 2056–2072. <https://doi.org/10.1053/j.gastro.2018.12.038>.
36. Burdette, D.L., and Vance, R.E. (2013). STING and the innate immune response to nucleic acids in the cytosol. *Nat. Immunol.* 14, 19–26. <https://doi.org/10.1038/ni.2491>.
37. Kwon, J., and Bakhour, S.F. (2020). The cytosolic DNA-sensing cGAS-STING pathway in cancer. *Cancer Discov.* 10, 26–39. <https://doi.org/10.1158/2159-8290.CD-19-0761>.
38. Jiang, M., Chen, P., Wang, L., Li, W., Chen, B., Liu, Y., Wang, H., Zhao, S., Ye, L., He, Y., and Zhou, C. (2020). cGAS-STING, an important pathway in cancer immunotherapy. *J. Hematol. Oncol.* 13, 81. <https://doi.org/10.1186/s13045-020-00916-z>.
39. Tan, Y.S., Sansanaphongpricha, K., Xie, Y., Donnelly, C.R., Luo, X., Heath, B.R., Zhao, X., Bellile, E., Hu, H., Chen, H., et al. (2018). Mitigating SOX2-potentiated immune escape of head and neck squamous cell carcinoma with a STING-inducing nanosatellite vaccine. *Clin. Cancer Res.* 24, 4242–4255. <https://doi.org/10.1158/1078-0432.CCR-17-2807>.
40. Ding, L., Kim, H.J., Wang, Q., Kearns, M., Jiang, T., Ohlson, C.E., Li, B.B., Xie, S., Liu, J.F., Stover, E.H., et al. (2018). PARP inhibition elicits STING-dependent antitumor immunity in brca1-deficient ovarian cancer. *Cell Rep.* 25, 2972–2980.e5. <https://doi.org/10.1016/j.celrep.2018.11.054>.
41. Fuertes, M.B., Woo, S.R., Burnett, B., Fu, Y.X., and Gajewski, T.F. (2013). Type I interferon response and innate immune sensing of cancer. *Trends Immunol.* 34, 67–73. <https://doi.org/10.1016/j.it.2012.10.004>.

42. Chen, Q., Boire, A., Jin, X., Valiente, M., Er, E.E., Lopez-Soto, A., Jacob, L., Patwa, R., Shah, H., Xu, K., et al. (2016). Carcinoma-astrocyte gap junctions promote brain metastasis by cGAMP transfer. *Nature* 533, 493–498. <https://doi.org/10.1038/nature18268>.
43. Lemos, H., Mohamed, E., Huang, L., Ou, R., Pacholczyk, G., Arbab, A.S., Munn, D., and Mellor, A.L. (2016). STING promotes the growth of tumors characterized by low antigenicity via IDO activation. *Cancer Res.* 76, 2076–2081. <https://doi.org/10.1158/0008-5472.CAN-15-1456>.
44. Ahn, J., Xia, T., Konno, H., Konno, K., Ruiz, P., and Barber, G.N. (2014). Inflammation-driven carcinogenesis is mediated through STING. *Nat. Commun.* 5, 5166. <https://doi.org/10.1038/ncomms6166>.
45. Tanaka, Y., and Chen, Z.J. (2012). STING specifies IRF3 phosphorylation by TBK1 in the cytosolic DNA signaling pathway. *Sci. Signal.* 5, ra20. <https://doi.org/10.1126/scisignal.2002521>.
46. Abe, T., and Barber, G.N. (2014). Cytosolic-DNA-mediated, STING-dependent proinflammatory gene induction necessitates canonical NF- κ B activation through TBK1. *J. Virol.* 88, 5328–5341. <https://doi.org/10.1128/JVI.00037-14>.
47. Khoo, L.T., and Chen, L.Y. (2018). Role of the cGAS-STING pathway in cancer development and oncotherapeutic approaches. *EMBO Rep.* 19, e46935. <https://doi.org/10.15252/embr.201846935>.
48. Corrales, L., Glickman, L.H., McWhirter, S.M., Kanne, D.B., Sivick, K.E., Katibah, G.E., Woo, S.R., Lemmens, E., Banda, T., Leong, J.J., et al. (2015). Direct activation of STING in the tumor microenvironment leads to potent and systemic tumor regression and immunity. *Cell Rep.* 11, 1018–1030. <https://doi.org/10.1016/j.celrep.2015.04.031>.
49. Tan, H.Y., Wang, N., Man, K., Tsao, S.W., Che, C.M., and Feng, Y. (2015). Autophagy-induced RelB/p52 activation mediates tumour-associated macrophage repolarisation and suppression of hepatocellular carcinoma by natural compound baicalin. *Cell Death Dis.* 6, e1942. <https://doi.org/10.1038/cddis.2015.271>.
50. Liu, M., O'Connor, R.S., Trefely, S., Graham, K., Snyder, N.W., and Beatty, G.L. (2019). Metabolic rewiring of macrophages by CpG potentiates clearance of cancer cells and overcomes tumor-expressed CD47-mediated 'don't-eat-me' signal. *Nat. Immunol.* 20, 265–275. <https://doi.org/10.1038/s41590-018-0292-y>.
51. Jaynes, J.M., Sable, R., Ronzetti, M., Bautista, W., Knotts, Z., Abisoye-Ogunniyan, A., Li, D., Calvo, R., Dashnyam, M., Singh, A., et al. (2020). Mannose receptor (CD206) activation in tumor-associated macrophages enhances adaptive and innate antitumor immune responses. *Sci. Transl. Med.* 12, eaax6337. <https://doi.org/10.1126/scitranslmed.aax6337>.
52. Beatty, G.L., Chiorean, E.G., Fishman, M.P., Saboury, B., Teitelbaum, U.R., Sun, W., Huhn, R.D., Song, W., Li, D., Sharp, L.L., et al. (2011). CD40 agonists alter tumor stroma and show efficacy against pancreatic carcinoma in mice and humans. *Science* 331, 1612–1616. <https://doi.org/10.1126/science.1198443>.
53. Cheng, T., Wang, M., Chen, L., Guo, Y., Chen, Z., and Wu, J. (2018). Increased expression of CD40/TRAFF1 and activation of nuclear factor- κ B-dependent proinflammatory gene expression in collagen-induced arthritis. *Scand. J. Rheumatol.* 47, 455–460. <https://doi.org/10.1080/03009742.2018.1432684>.
54. Dougan, M., Li, D., Neuberg, D., Mihm, M., Googe, P., Wong, K.K., and Dranoff, G. (2011). A dual role for the immune response in a mouse model of inflammation-associated lung cancer. *J. Clin. Invest.* 121, 2436–2446. <https://doi.org/10.1172/JCI44796>.
55. Wente, M.N., Mayer, C., Gaida, M.M., Michalski, C.W., Giese, T., Bergmann, F., Giese, N.A., Büchler, M.W., and Friess, H. (2008). CXCL14 expression and potential function in pancreatic cancer. *Cancer Lett.* 259, 209–217. <https://doi.org/10.1016/j.canlet.2007.10.021>.
56. Pramanik, K.C., Makenna, M.R., Bhowmick, K., and Pandey, M.K. (2018). Advancement of NF- κ B signaling pathway: a novel target in pancreatic cancer. *Int. J. Mol. Sci.* 19, 3890. <https://doi.org/10.3390/ijms19123890>.
57. Faridi, M.H., Khan, S.Q., Zhao, W., Lee, H.W., Altintas, M.M., Zhang, K., Kumar, V., Armstrong, A.R., Carmona-Rivera, C., Dorschner, J.M., et al. (2017). CD11b activation suppresses TLR-dependent inflammation and autoimmunity in systemic lupus erythematosus. *J. Clin. Invest.* 127, 1271–1283. <https://doi.org/10.1172/JCI88442>.
58. Jiang, H., Hegde, S., Knolhoff, B.L., Zhu, Y., Herndon, J.M., Meyer, M.A., Nywening, T.M., Hawkins, W.G., Shapiro, I.M., Weaver, D.T., et al. (2016). Targeting focal adhesion kinase renders pancreatic cancers responsive to checkpoint immunotherapy. *Nat. Med.* 22, 851–860. <https://doi.org/10.1038/nm.4123>.
59. Lander, V.E., Belle, J.I., Kingston, N.L., Herndon, J.M., Hogg, G.D., Liu, X., Kang, L.I., Knolhoff, B.L., Bogner, S.J., Baer, J.M., et al. (2022). Stromal reprogramming by FAK inhibition overcomes radiation resistance to allow for immune priming and response to checkpoint blockade. *Cancer Discov.* 12, 2774–2799. <https://doi.org/10.1158/2159-8290.CD-22-0192>.
60. Hingorani, S.R., Petricoin, E.F., Maitra, A., Rajapakse, V., King, C., Jacobetz, M.A., Ross, S., Conrads, T.P., Veenstra, T.D., Hitt, B.A., et al. (2003). Preinvasive and invasive ductal pancreatic cancer and its early detection in the mouse. *Cancer Cell* 4, 437–450. [https://doi.org/10.1016/s1535-6108\(03\)00309-x](https://doi.org/10.1016/s1535-6108(03)00309-x).
61. Morton, J.P., Timpson, P., Karim, S.A., Ridgway, R.A., Athineos, D., Doyle, B., Jamieson, N.B., Oien, K.A., Lowy, A.M., Brunton, V.G., et al. (2010). Mutant p53 drives metastasis and overcomes growth arrest/senescence in pancreatic cancer. *Proc Natl Acad Sci U S A* 107, 246–251.
62. Kim, M.P., Evans, D.B., Wang, H., Abbruzzese, J.L., Fleming, J.B., and Gallick, G.E. (2009). Generation of orthotopic and heterotopic human pancreatic cancer xenografts in immunodeficient mice. *Nat. Protoc.* 4, 1670–1680. <https://doi.org/10.1038/nprot.2009.171>.
63. Borcherding, N., Vishwakarma, A., Voigt, A.P., Bellizzi, A., Kaplan, J., Nepple, K., Salem, A.K., Jenkins, R.W., Zakharia, Y., and Zhang, W. (2021). Mapping the immune environment in clear cell renal carcinoma by single-cell genomics. *Commun. Biol.* 4, 122. <https://doi.org/10.1038/s42003-020-01625-6>.
64. Yost, K.E., Satpathy, A.T., Wells, D.K., Qi, Y., Wang, C., Kageyama, R., McNamara, K.L., Granja, J.M., Sarin, K.Y., Brown, R.A., et al. (2019). Clonal replacement of tumor-specific T cells following PD-1 blockade. *Nat. Med.* 25, 1251–1259. <https://doi.org/10.1038/s41591-019-0522-3>.
65. Wu, T.D., Madireddi, S., de Almeida, P.E., Banchereau, R., Chen, Y.J.J., Chitre, A.S., Chiang, E.Y., Iftikhar, H., O'Gorman, W.E., Au-Yeung, A., et al. (2020). Peripheral T cell expansion predicts tumour infiltration and clinical response. *Nature* 579, 274–278. <https://doi.org/10.1038/s41586-020-2056-8>.
66. Zheng, Y., Chen, Z., Han, Y., Han, L., Zou, X., Zhou, B., Hu, R., Hao, J., Bai, S., Xiao, H., et al. (2020). Immune suppressive landscape in the human esophageal squamous cell carcinoma microenvironment. *Nat. Commun.* 11, 6268. <https://doi.org/10.1038/s41467-020-20019-0>.
67. Leader, A.M., Grout, J.A., Maier, B.B., Nabet, B.Y., Park, M.D., Tabachnikova, A., Chang, C., Walker, L., Lansky, A., Le Berichel, J., et al. (2021). Single-cell analysis of human non-small cell lung cancer lesions refines tumor classification and patient stratification. *Cancer Cell* 39, 1594–1609.e12. <https://doi.org/10.1016/j.ccel.2021.10.009>.
68. Steele, N.G., Carpenter, E.S., Kemp, S.B., Sirihorachai, V.R., The, S., Delrosario, L., Lazarus, J., Amir, E.A.D., Gunchick, V., Espinoza, C., et al. (2020). Multimodal mapping of the tumor and peripheral blood immune landscape in human pancreatic cancer. *Nat. Cancer* 1, 1097–1112. <https://doi.org/10.1038/s43018-020-00121-4>.
69. Wu, S.Z., Al-Eryani, G., Roden, D.L., Junankar, S., Harvey, K., Andersson, A., Thennavan, A., Wang, C., Torpy, J.R., Bartonicek, N., et al. (2021). A single-cell and spatially resolved atlas of human breast cancers. *Nat. Genet.* 53, 1334–1347. <https://doi.org/10.1038/s41588-021-00911-1>.
70. Laumont, C.M., Wouters, M.C.A., Smazynski, J., Gierc, N.S., Chavez, E.A., Chong, L.C., Thornton, S., Milne, K., Webb, J.R., Steidl, C., and Nelson, B.H. (2021). Single-cell profiles and prognostic impact of tumor-infiltrating lymphocytes coexpressing CD39, CD103, and PD-1 in ovarian cancer. *Clin. Cancer Res.* 27, 4089–4100. <https://doi.org/10.1158/1078-0432.CCR-20-4394>.

71. Hao, Y., Hao, S., Andersen-Nissen, E., Mauck, W.M., 3rd, Zheng, S., Butler, A., Lee, M.J., Wilk, A.J., Darby, C., Zager, M., et al. (2021). Integrated analysis of multimodal single-cell data. *Cell* 184, 3573–3587.e29. <https://doi.org/10.1016/j.cell.2021.04.048>.
72. Andreatta, M., Berenstein, A.J., and Carmona, S.J. (2022). scGate: marker-based purification of cell types from heterogeneous single-cell RNA-seq datasets. *Bioinformatics* 38, 2642–2644. <https://doi.org/10.1093/bioinformatics/btac141>.
73. Korsunsky, I., Millard, N., Fan, J., Slowikowski, K., Zhang, F., Wei, K., Baglaenko, Y., Brenner, M., Loh, P.R., and Raychaudhuri, S. (2019). Fast, sensitive and accurate integration of single-cell data with Harmony. *Nat. Methods* 16, 1289–1296. <https://doi.org/10.1038/s41592-019-0619-0>.
74. Andreatta, M., and Carmona, S.J. (2021). UCell: robust and scalable single-cell gene signature scoring. *Comput. Struct. Biotechnol. J.* 19, 3796–3798. <https://doi.org/10.1016/j.csbj.2021.06.043>.
75. Liberzon, A., Birger, C., Thorvaldsdóttir, H., Ghandi, M., Mesirov, J.P., and Tamayo, P. (2015). The Molecular Signatures Database (MSigDB) hallmark gene set collection. *Cell Syst.* 1, 417–425. <https://doi.org/10.1016/j.cels.2015.12.004>.
76. Zuo, C., Baer, J.M., Knolhoff, B.L., Belle, J.I., Liu, X., Alarcon De La Lastra, A., Fu, C., Hogg, G.D., Kingston, N.L., Breden, M.A., et al. (2023). Stromal and therapy-induced macrophage proliferation promotes PDAC progression and susceptibility to innate immunotherapy. *J. Exp. Med.* 220, e20212062. <https://doi.org/10.1084/jem.20212062>.
77. Wu, T., Hu, E., Xu, S., Chen, M., Guo, P., Dai, Z., Feng, T., Zhou, L., Tang, W., Zhan, L., et al. (2021). clusterProfiler 4.0: a universal enrichment tool for interpreting omics data. *Innovation* 2, 100141. <https://doi.org/10.1016/j.xinn.2021.100141>.
78. Zhu, Y., Knolhoff, B.L., Meyer, M.A., Nywening, T.M., West, B.L., Luo, J., Wang-Gillam, A., Goedegebuure, S.P., Linehan, D.C., and DeNardo, D.G. (2014). CSF1/CSF1R blockade reprograms tumor-infiltrating macrophages and improves response to T-cell checkpoint immunotherapy in pancreatic cancer models. *Cancer Res.* 74, 5057–5069. <https://doi.org/10.1158/0008-5472.CAN-13-3723>.
79. Bronner, D.N., and O'Riordan, M.X. (2016). Measurement of mitochondrial DNA release in response to ER stress. *Bio. Protoc.* 6, e1839. <https://doi.org/10.21769/BioProtoc.1839>.

STAR★METHODS

KEY RESOURCES TABLE

REAGENT or RESOURCE	SOURCE	IDENTIFIER
Antibodies		
anti-mouse CD44 (IM7)	Leinco	Cat# C382 RRID: AB_2737485
anti-mouse GITR (DTA-1)	BioXcell	Cat# BE0063 RRID: AB_1107688
anti-mouse CD25 (PC61)	Leinco	Cat# C1194 RRID: AB_2737451
anti-mouse CD38 (90)	eBioscience	Cat# 14-0381-82 RRID: AB_467219
anti-mouse CD90 (G7)	Biolegend	Cat# 105202 RRID: AB_313169
anti-mouse Lag-3 (C9B7W)	Leinco	Cat# L306 RRID: AB_2737552
anti-mouse CD27 (LG.7F9)	eBioscience	Cat# 50-124-94
anti-mouse KLRG1 (2F1/KLRG1)	BioXcell	Cat# BE0201 RRID: AB_10949054
anti-mouse CD103 (2E7)	Biolegend	Cat# 121402 RRID: AB_535945
anti-mouse CD4 (GK1.5)	BioXcell	Cat# BE0003-1 RRID: AB_1107636
anti-mouse CD45 (30-F11)	Fluidigm	Cat# 3089005B RRID: AB_2651152
anti-mouse CD62L (MEL-14)	Leinco	Cat# C2118 RRID: AB_2737457
anti-mouse ICOS (C398.4A)	eBioscience	Cat# 14-9949-82 RRID: AB_468637
anti-mouse OX-40 (OX-86)	BioXcell	Cat# BE0031 RRID: AB_1107592
anti-mouse PD-1 (RMP1-30)	eBioscience	Cat# 14-9981-82 RRID: AB_468655
anti-mouse TIGIT (1G9)	BioXcell	Cat# BE0274 RRID: AB_2687797
anti-mouse CD69 (H1.2F3)	eBioscience	Cat# 14-0691-82 RRID: AB_467325
anti-mouse TCR β (H57-597)	BioXcell	Cat# BE0102 RRID: AB_10950158
anti-mouse CD127 (A7R34)	BioXcell	Cat# BE0065 RRID: AB_1107590
anti-mouse CD39 (Duha59)	Biolegend	Cat# 143802 RRID: AB_11204243
anti-mouse NK1.1 (PK136)	BioXcell	Cat# BE0036 RRID: AB_1107737
anti-mouse CD8 α (53-6.7)	Leinco	Cat# C375 RRID: AB_2737478
anti-mouse TCR $\gamma\delta$ (GL3)	eBioscience	Cat# 14-5711-82 RRID: AB_467569
anti-mouse Tim3 (RMT3-23)	BioXcell	Cat# BE0115 RRID: AB_10949464

(Continued on next page)

Continued

REAGENT or RESOURCE	SOURCE	IDENTIFIER
anti-mouse FoxP3 (FJK-16s)	eBioscience	Cat# 14-5773-82 RRID: AB_467576
anti-mouse GATA3 (TWAJ)	eBioscience	Cat# 14-9966-82 RRID: AB_1210519
anti-mouse GranzymeB (GB11)	eBioscience	Cat# MA1-80734 RRID: AB_931084
anti-mouse CTLA-4 (UC10-4B9)	eBioscience	Cat# 50-129-16
anti-mouse Ki67 (8D5)	Novus	Cat# NBP2-22112
anti-mouse TCF1 (812145)	R&D	Cat# MAB8224
anti-mouse ROR- γ t (AFKJS-9)	eBioscience	Cat# 14-6988-82 RRID: AB_1834475
anti-mouse Eomes (Dan11mag)	eBioscience	Cat# 50-245-556
anti-mouse T-bet (4B10)	Biolegend	Cat# 644802 RRID: AB_1595503
anti-mouse CD45 (30-F11)	Fluidigm	Cat# 3089005B RRID: AB_2651152
anti-mouse Ki67 (8D5)	Novus	Cat# NBP2-22112
anti-mouse CD11c (N418)	Fluidigm	Cat# 3142003B RRID: AB_2814737
anti-mouse CD68 (FA-11)	Biolegend	Cat# 137001 RRID: AB_2044003
anti-mouse MHC-I (28-14-8)	Fluidigm	Cat# 3144016B RRID: AB_2687831
anti-mouse CD206 (C068C2)	Biolegend	Cat# 141702 RRID: AB_10900233
anti-mouse F4/80 (BM8)	Fluidigm	Cat# 3146008B RRID: AB_2895117
anti-mouse MHC-II (M5/114.15.2)	Biolegend	Cat# 107602 RRID: AB_313317
anti-mouse CD11b (M1/70)	Fluidigm	Cat# 3148003B RRID: AB_2814738
anti-mouse CD172 α /SIRP α (P84)	Biolegend	Cat# 144002 RRID: AB_11203711
anti-mouse Ly6C (HK1.4)	Fluidigm	Cat# 3150010B RRID: AB_2895118
anti-mouse Ly6G (1A8)	Fluidigm	Cat# 3151010B
anti-mouse CD64 (X54-5/7.1)	Biolegend	Cat# 139301 RRID: AB_10612757
anti-mouse Tim4 (RMT4-54)	Biolegend	Cat# 130002 RRID: AB_1227802
anti-mouse XCR1(Zet)	Biolegend	Cat# 148202 RRID: AB_2563841
anti-mouse CD103 (2E7)	Biolegend	Cat# 121402 RRID: AB_535945
anti-mouse NK1.1 (PK136)	BioXcell	Cat# BE0036 RRID: AB_1107737
anti-mouse Bst2 (120G8)	Novous/imgenx	Cat# DDX0390P-100 RRID: AB_2827525
anti-mouse IRF4 (3E4)	Biolegend	Cat# 646402 RRID: AB_2280462
anti-mouse CD39 (Duha59)	Biolegend	Cat# 143802 RRID: AB_11204243

(Continued on next page)

Continued

REAGENT or RESOURCE	SOURCE	IDENTIFIER
anti-mouse NK1.1 (PK136)	BioXcell	Cat# BE0036 RRID: AB_1107737
anti-mouse CD83 (Michel-17)	thermofisher scientific	Cat# 14-0831-82 RRID: AB_467357
anti-mouse CD40 (HM40-3)	Fluidigm	Cat# 124601 RRID: AB_1134239
anti-mouse Ox40L (RM134L)	Biolegend	Cat# 108802 RRID: AB_313401
anti-mouse CCR2 (475301)	R&D systems	Cat# MAB55381-100 RRID: AB_2749828
anti-mouse Cx3CR1(SA011F11)	Fluidigm	Cat# 3164023B RRID: AB_2832247
anti-mouse CCR7 (4B12)	Biolegend	Cat# 120101 RRID: AB_389229
anti-mouse PDL2 (TY25)	BioXCell	Cat# BE0112 RRID: AB_10950106
anti-mouse VISTA (MIH63)	Biolegend	Cat# 150202 RRID: AB_2565897
anti-mouse Tim3 (RMT3-23)	BioXcell	Cat# BE0115 RRID: AB_10949464
anti-mouse PD-L1 (10F.9G2)	BioXCell	Cat# BE0101 RRID: AB_10949073
anti-mouse CD80 (16-10A1)	Biolegend	Cat# 104702 RRID: AB_313123
anti-mouse CD135/FLT3 (A2F10)	Thermo Fisher Scientific	Cat# 14-1351-82 RRID: AB_467481
anti-mouse CD86 (GL1)	Fluidigm	Cat# 3172016B RRID: AB_2922923
anti-mouse B220 (RA3-682)	Fluidigm	Cat# 3144011B RRID: AB_2811239
anti-mouse CD45 (30-F11)	eBioscience	Cat# 25-0451-82 RRID: AB_2734986
anti-mouse CD45 (30-F11)	BD Biosciences	Cat# 564225 RRID: AB_2716861
anti-mouse CD45 (30-F11)	BioLegend	Cat# 103184
anti-mouse CD45 (30-F11)	Invitrogen	Cat# 63-045-182
anti-mouse CD3e (145-2C11)	eBioscience	Cat# 17-0031-82 RRID: AB_469315
anti-mouse CD3e (145-2C11)	BD Biosciences	Cat# 563123 RRID: AB_2687954
anti-mouse CD4 (RM4-4)	eBioscience	Cat# 11-0043-82 RRID: AB_464900
anti-mouse CD4 (RM4-4)	BioLegend	Cat# 116022 RRID: AB_2715958
anti-mouse CD8 α (53-6.7)	BD Biosciences	Cat# 563786 RRID: AB_2732919
anti-mouse CD8 α (53-6.7)	BD Biosciences	Cat# 553035 RRID: AB_398527
anti-mouse Foxp3 (FJK-16s)	eBioscience	Cat# 15-5773-82 RRID: AB_468806
anti-mouse CD19 (eBio1D3)	eBioscience	Cat# 17-0193-82 RRID: AB_1659676
anti-mouse CD11b (M1/70)	eBioscience	Cat# 56-0112-82 RRID: AB_657585

(Continued on next page)

Continued

REAGENT or RESOURCE	SOURCE	IDENTIFIER
anti-mouse CD11b (M1/70)	Invitrogen	Cat# 56-0112-82 RRID: AB_657585
anti-mouse Ly6C (HK1.4)	eBioscience	Cat# 45-5932-82 RRID: AB_2723343
anti-mouse Ly6C (HK1.4)	BioLegend	Cat# 128006 RRID: AB_1186135
anti-mouse Ly6G (1A8)	BioLegend	Cat# 127608 RRID: AB_1186099
anti-mouse Ly6G (1A8)	BioLegend	Cat# 127614 RRID: AB_2227348
anti-mouse F4/80 (BM8)	eBioscience	Cat# 15-4801-82 RRID: AB_468798
anti-mouse F4/80 (BM8)	Invitrogen	Cat# 25-4801-82 RRID: AB_469653
anti-mouse MHC-II (M5/115.15.2)	eBioscience	Cat# 48-5321-82 RRID: AB_1272204
anti-mouse MHC-II (I-A/I-E) (M5/114.15.2)	Invitrogen	Cat# 58-5321-82 RRID: AB_2811913
anti-mouse Ki67 (SolA15)	eBioscience	Cat# 50-5698-82 RRID: AB_2574235
anti-mouse SIINFEKL Dextramer (N/A)	Immudex	Cat# JD2163
anti-mouse Granzyme B (GB11)	BD Horizon	Cat# 563388 RRID: AB_2738174
anti-mouse IFN γ (XMG1.2)	BioLegend	Cat# 505808 RRID: AB_315402
anti-mouse TNF α (MP6-XT22)	eBioscience	Cat# 11-7321-82 RRID: AB_465418
CD11b (EPR1344)	Abcam	Cat# ab13357 RRID: AB_2650514
F4/80 (D2S9R)	Cell Signaling	Cat# 70076 RRID: AB_2799771
STING (D2P2F)	Cell Signaling	Cat# 13647 RRID: AB_2732796
NF κ B p65 (D14E12)	Cell Signaling	Cat# 8242 RRID: AB_10859369
pSTAT1 (D3B7)	Cell Signaling	Cat# 8826 RRID: AB_2773718
CK19 (Troma III)	DSHB	Cat# Uoflawa DSHB TROMA-III C
CD8 (D4W2Z)	Cell Signaling	Cat# 98941 RRID: AB_2756376
CD8 (SP16)	Invitrogen	Cat# MA5-14548 RRID: AB_10984334
CD163 (10D6)	Leica Biosystem	Cat# NCL-L-CD163 RRID: AB_2756375
Keratin17/19 (D4G2)	Cell Signaling	Cat# 12434 RRID: AB_2797912
Cytokeratin, Muti (AE1/AE3)	Leica Biosystem	Cat# NCL-L-AE1/AE3-601 RRID: AB_2924990
pAKT (D9E)	Cell Signaling	Cat# 4060 RRID: AB_2315049
pIRF3 (D6O1M)	Cell Signaling	Cat# 29047 RRID: AB_2773013
IRF3 (D83B9)	Cell Signaling	Cat# 4302

(Continued on next page)

Continued

REAGENT or RESOURCE	SOURCE	IDENTIFIER
STAT1 (D1K9Y)	Cell Signaling	Cat# 14994 RRID: AB_2737027
pFAK	Cell Signaling	Cat# 3283 RRID: AB_2173659
FAK	Cell Signaling	Cat# 3285 RRID: AB_2269034
pp65 (93H1)	Cell Signaling	Cat# 3033 RRID: AB_331284
pIκB α (14D4)	Cell Signaling	Cat# 2859 RRID: AB_561111
IκB α	Cell Signaling	Cat# 9242 RRID: AB_331623
Cleaved Caspase-3 (Asp175)	Cell Signaling	Cat# 9661 RRID: AB_2341188
Ubiquitin (E4I2J)	Cell Signaling	Cat# 43124 RRID: AB_2799235
SIRT3 (D22A3)	Cell Signaling	Cat# 5490 RRID: AB_10828246
β -ACTIN (13E5)	Cell Signaling	Cat# 4970 RRID: AB_2223172
IFN β	Invitrogen	Cat# PA5-20390 RRID: AB_11155641
CXCL10 (10H11L3)	Invitrogen	Cat# 701225 RRID: AB_2532429
Oligonucleotides		
Primers and siRNA used in this study are list in Table S6	This paper	N/A
Biological samples		
Human PDAC TMA	Washington University	IRB# 201704078
Tumor biopsies	Gossamer Bio	# NTC04060342
Cultrex Basement membrane extract, Pathclear	Trevigen	Cat# 3432-001-01
Chemicals, peptides, and recombinant proteins		
STING agonist (ML-RR-S2 CDA; ADU-S100)	MedChemExpress	Cat# HY-12885B
Gemcitabine hydrochloride	Ark Pharm	Cat# 122111-03-9
Paclitaxel	Fresenius Kabi	#00363323763503
InVivoMAb anti-mouse IL-1R (CD121a) (JAMA-147)	BioXCell	Cat# BE0256
InVivoMAb anti-mouse CD4 (GK1.5)	BioXCell	Cat# BE0003-1
InVivoMAb anti-mouse CD8 (2.43)	BioXCell	Cat# BP0061
ODN 1585 -TLR9 ligand	InvivoGen	Cat# tlr1-1585
R848 (Resiquimod)	InvivoGen	Cat# tlr1-r848-5
Autophagy inhibitor, 3-MA	Sigma-Aldrich	Cat# 5142-23-4
N-acetyl-L-cysteine	Sigma-Aldrich	Cat# 616-91-1
2'3'- ethidium bromide solution	Invitrogen	Cat# 17898
MG132	MedChemExpress	Cat# HY-13259
Collagenase A	Sigma/Roche	Cat# 10103586001
DNAse I	Sigma	Cat# 11284932001
Cell Stimulation cocktail (PMA/Iono)	Ebioscience	Cat# 00-4970-93
Brefeldin A	Biolegend	Cat# 420601
Monensin	Biolegend	Cat# 420701
2'-7'-dichlorodihydrofluorescein diacetate	Sigma-Aldrich	Cat# 287810

(Continued on next page)

Continued

REAGENT or RESOURCE	SOURCE	IDENTIFIER
Critical commercial assays		
E.Z.N.A. Total RNA kit I	Omega	Cat# R6834-02
qScript cDNA Supermix kit	Quantabio	Cat# 95048-500
Taqman Gene Expression Master Mix	Thermo Fisher	Cat# 4370074
BOND Polymer Refine Detection kit Leica #DS9800	Leica	Cat# DS9800
BOND Intense R Detection kit	Leica	Cat# DS9263
Cytofix kit	BD Bioscience	Cat# 554655
CSF1 neutralizing antibody (Clone 5A1)	BioXCell	Cat# BE0204
PBS Liposomes & Clodronate Liposomes	Liposoma	Cat# CP-005-005
Halt Protease and Phosphatase Inhibitor	Thermo Scientific	Cat# 78442
RIPA Buffer(10x)	Cell Signaling	Cat# UN3082
Mouse Macrophage Nucleofector Kit	Lonza	Cat# VPA-1009
Pierce BCA Protein Assay Kit	Thermo Scientific	Cat# 23225
Recombinant Murine M-CSF	PeproTech	Cat# 315-02
Mouse IFN-beta DuoSet ELISA	R&D Systems	Cat# DY8234-05
Mouse IL-1 beta/IL-1F2 DuoSet ELISA	R&D Systems	Cat# DY401
IP-10/CXCL10 Mouse Matched Antibody Pair	Invitrogen	Cat# BMS6018MST
I-TAC/CXCL11 Mouse ELISA Kit	Invitrogen	Cat# EMCXCL11
protein A agarose Beads	Cell Signaling Technology	Cat# 9863
NucleoSpin Tissue Kit	Takara Bio	Cat# 740952.50
SuperSignalTM West Dura Extended Duration Substrate	Thermo Fisher Scientific	Cat# 34076
CellTiter96 Non-Radioactive Cell Proliferation Assay	Promega	Cat# G4002
EasySep Human CD14 Selection Kit	Stemcell Technologies	Cat# 17858
Pierce™ Protein Concentrator PES, 3K MWCO	Thermo Fisher Scientific	Cat# 88525
Experimental models: Cell lines		
KP2/KP1; derived from a KPC tumor	This paper; Jiang et al. 2016 ⁵⁸	N/A
KI; derived from Kras-Ink mouse	This paper; Jiang et al. 2016 ⁵⁸	N/A
KP2-OVA-GFP; generated from KP2 cells transduced with OVA-GFP containing lentivirus and sorted for GFP	This paper; VE Lander et al. 2022 ⁵⁹	N/A
Panc-1	obtained from Dr. Kian H from ATCC	RRID: CVCL_0480
Capan-1	obtained from Dr. Kian H from ATCC	RRID: CVCL_0237
CFPAC-1	obtained from Dr. Kian H from ATCC	RRID: CVCL_1119
HPAC	obtained from Dr. Kian H from ATCC	RRID: CVCL_3517
Experimental models: Organisms/strains		
mouse: p48-Cre;Kras ^{LSL-G12D} ,Trp53 ^{fl/fl}	Hingorani et al., 2003; ⁶⁰ Morton et al., 2010 ⁶¹	N/A
mouse: C57BL/6J	The Jackson Laboratory	Stock# 000664
mouse: FVB/NCr	Charles River Laboratories	Strain# 559
mouse: B6.129S4- <i>Itgam</i> ^{tm1Myd} /J	The Jackson Laboratory	Strain# 003991
mouse: B6(Cg)- <i>Sting1</i> ^{tm1.2Camb} /J	The Jackson Laboratory	Strain# 025805
mouse: C57BL/6-Tlrgem1.1Ldm/j	The Jackson Laboratory	Strain# 034449

(Continued on next page)

Continued

REAGENT or RESOURCE	SOURCE	IDENTIFIER
Deposited data		
scRNASeq data	This paper	GSE220959
Software and algorithms		
Flowjo v10.7.2	Flowjo, L.L.C.	Flowjo, L.L.C. RRID:SCR_008520
Prism v9	Graphpad	www.graphpad.com RRID:SCR_000306
Docker	Rocker/rstudio:latest cumulusprod/cellranger:4.0.0	https://hub.docker.com/r rocker/rstudio https://hub.docker.com/r cumulusprod/cellranger/tags
HALO v3.2.1851	Indica Labs-High Plex Fv4.0.3 Indica Labs-Deconvolution v1.0.4	https://indicalab.com/products/high-plex-fl/
Cytobank	Cytobank, Inc	Wustl.cytobank.org
FACSDiva	BD Biosciences	RRID: SCR_001456
Zen	Zeiss	Zeiss.com
Fiji v2.0.0	ImageJ	
R v3.6.3	R Core Team Clusterprofiler Seurat v 3.2.0 Harmony CATALYST	https://cran.r-project.org/bin/windows/base/old/3.6.3/ https://github.com/YuLab-SMU/clusterProfiler https://satijalab.org/seurat/ https://github.com/immunogenomics/harmony https://github.com/HelenaLC/CATALYST

RESOURCE AVAILABILITY

Lead contact

Further information and requests for resources and reagents should be directed to and will be fulfilled by the lead contact, David G. DeNardo (ddenardo@wustl.edu).

Materials availability

This study did not generate new unique reagents.

Data and code availability

The scRNA sequencing data from PDAC lesions were found at the Gene Expression Omnibus Repository (GEO) accession number GSE220959. All software packages used are publicly available through commercial vendors.

EXPERIMENTAL MODEL AND SUBJECT DETAILS

Human tumor tissue

TMA studies were conducted on surgically resected PDAC specimens from patients diagnosed at the Department of Pathology at Washington University (St. Louis, MO, USA). To assemble TMAs, clearly defined areas of tumor tissues were demarcated, and two biopsies (1.0 mm in diameter) were taken from each donor block. Four μ m paraffin sections were used for multiple immunohistochemistry analyses. All human tissue studies were approved by the Washington University School of Medicine Ethics Committee in accordance with recognized ethical guidelines (IRB# 201704078). Fully automated image acquisition was performed using a Zeiss Axio Scan Z1 Slide Scanner system with a 20 \times objective (Carl Zeiss, Jena, Germany) to capture whole slide digital images.

Human tumor biopsy sections from the Phase 1 first-in-human clinical trial evaluating GB1275 as monotherapy (Regimen A) and in combination with pembrolizumab (Regimen B) in specified advanced tumors (NCT04060342) were provided by Gossamer Bio.³² Following informed consent, core tissue biopsies were obtained from pre- and post-GB1275 doses from 11 patients. Post-treatment biopsies were obtained prior to week 8 of treatment. For details on tumor type and treatment, see Table S5. Tissues were fixed (10% neutral-buffered formalin, 48 hours) and embedded in paraffin immediately after biopsy. Needle core biopsies were fixed for a minimum of 8 hours.

The genetic mouse PDAC model and other mouse models

KPC (p48-Cre; LSL-Kras^{G12D/wt}; p53^{Flox/Flox}) mice were bred in-house, and C57BL/6 breeders were obtained from the Jackson Laboratory (Bar Harbor, ME, USA). KPC mice were backcrossed to C57BL/6 over six generations and validated as C57BL/6 congenic through single nucleotide polymorphism scanning. The CD11b^{-/-}, STING^{-/-}, and TLR9^{-/-} mice (all on the C57BL/6 background) were purchased from Jackson Laboratories. Mice were maintained in the Washington University Laboratory for Animal Care barrier facility, and all studies involving animals were approved by the Washington University School of Medicine Institutional Animal Studies Committee (protocol #20190856).

Cell lines, pharmacologic compounds and *in vivo* antibodies

KP2/KP1 cells were derived from a KPC tumor obtained in-house. Kras-INK (KI) cells were derived from Pdx1-Cre/LSL-Kras^{G12D}/Ink^{ArF}^{Flox/Flox} mice.⁵⁸ KP2-OVA-GFP cells were generated from KP2 cells transduced with OVA-GFP containing lentivirus and sorted for GFP. Panc-1, Capan-1, CFPAC-1, and HPAC cells were obtained from Dr. Kian H. Lim's laboratory. All cell lines tested negative for MAP and mycoplasma. GB1275 was provided by Gossamer Bio (San Diego, CA, USA). For animal experiments, GB1275 was administrated at 60 or 120 mg/kg by oral gavage twice a day (BID). GB1275 was dosed at 60 mg/kg in experiments described in Figures 2A–2F and 120 mg/kg in all other *in vivo* experiments. For *in vitro* experiments, 10 μM GB1275 dissolved in dimethyl sulfoxide (DMSO) was used for BMDMs in most experiments. A total of 1 or 5 μM of GB1275 was used, as noted in the figure legends. STING agonist (ADU-S100) was purchased from MedChemExpress (Monmouth Junction, NJ, USA) and was administered at 25 μg/mouse by intratumoral injection every 4 days. For *in vitro* experiments, 10 nM ADU-S100 (dissolved in DMSO) was treated for BMDMs. Gemcitabine hydrochloride was purchased from Ark Pharm (Arlington Heights, IL, USA) and was administered at 50 mg/kg by intravenous injection (i.v.) every 5 days. Paclitaxel was purchased from Fresenius Kabi (Bad Homburg, Germany) and was administered at 10 mg/kg by i.v. every 5 days. InVivoMAb anti-mouse IL-1R (CD121a) was purchased from BioXCell (Lebanon, NH, USA) (Clone: JAMA-147, BE0256) and was administered at 200 μg/mouse, every 3 days by intraperitoneal injection (i.p.). For T cell depletion, CD4 or CD8 neutralizing IgG antibodies (αCD4 clone GK1.5; αCD8 clone 2.43, BioXCell) were administered, with the first injection (1 day before GB1275 treatment) containing 400 μg and subsequent injections (every 4 days) containing 200 μg of each IgG. ODN 1585 -TLR9 ligand and R848 (Resiquimod) (TLR7 agonist) were purchased from InvivoGen (San Diego, CA, USA) and administered at 50 μg/mouse by intratumoral injections every 5 days. For *in vitro* experiments, gemcitabine was treated at 1 or 10 μM (10 μM was used in Figure 6B, 1 and 10 μM were used in Figure S6A) dissolved in phosphate-buffered saline for BMDMs. Autophagy inhibitor, 3-MA was purchased from Sigma-Aldrich (St. Louis, MO, USA). The N-acetyl-L-cysteine was purchased from Sigma-Aldrich. VS4718 was used as a FAK1/PyTK2 inhibitor at 1.0 μM for Figure 4G and 0.5 μM for the rest experiment. The 2'3'-ethidium bromide solution was purchased from Invitrogen by Thermo Fisher Scientific (Waltham, MA, USA) and was treated as 1.5 mg/mL. MG132 was purchased from MedChemExpress and was treated as 10 μM dissolved in DMSO.

Syngeneic model and preclinical animal cohorts

Age-matched 6–8-week-old female C57BL/6 and FVB/NJ mice were used for orthotopic/transplantable mouse models. Syngeneic PDAC tumors were established by surgical implantation, as previously described.⁵⁸ Approximately, KP2 (200,000), KI (100,000), or KP2-OVA (200,000) cells in 50 μL of Cultrex (Trevigen, Gaithersburg, MD, USA) were injected into the pancreas of sex-matched C57BL/6 or FVB/NJ mice as previously described.⁶² Cohorts of mice were randomized into different treatment groups by gross palpation of tumors in the pancreas. In the transplantable model, KP2 (250,000) or KP2-OVA (250,000) cells in 50 μL of Cultrex (Trevigen, Gaithersburg, MD, USA) were injected into each mouse's back/flank or mammary fat pad (Figure 7L). Cohorts of mice were randomized into different treatment groups by tumor volume from external caliper measurements. Mice were maintained within the Washington University Laboratory for Animal Care barrier facility. All studies involving animals were approved by the Washington University School of Medicine Institutional Animal Studies Committee.

METHOD DETAILS

Tissue harvesting

Mice were euthanized by cardiac perfusion using 15 mL of PBS-heparin under isoflurane anesthesia. When taken for histology, tumor tissues were fixed in 10% neutral-buffered formalin overnight at 4°C. When taken for cellular assays, tumor tissues or respective lymph nodes were manually minced and digested in 15 mL of sterile 1× HBSS (Thermo Fisher Scientific) containing 2 mg/mL of collagenase A (Roche, Basel, Switzerland) and 1× DNase I (Sigma-Aldrich) for 30 min at 37°C with constant stirring. Digestion was quenched in 5 mL of sterile fetal bovine serum (FBS; Atlanta Biologicals, Flowery Branch, GA, USA), filtered through 40 μm nylon mesh, pelleted through centrifugation (2,000 rpm for 5 min at 4°C), and resuspended in the required media/buffer as single-cell suspensions.

Mass cytometry (CyTOF)

Tumors taken from KI orthotopic models were treated with vehicle or GB1275 for 12 days. Eight tumors from each group were pooled as four samples (two tumors were pooled as one sample). Mouse samples from the KP2 subcutaneous model were treated with GB1275, ADU-S100, or GB1275+ADU-S100 for 14 days. We used six individuals per group. Tumor samples were digested in HBSS supplemented with 2 mg/mL collagenase A (Roche) and DNase I at 37°C for 30 min with agitation to generate single-cell

suspensions. Cell suspensions were counted and stained in 5 μ M cisplatin per million cells for exactly 3 min on ice and washed with Cy-FACS buffer (PBS, 0.1% BSA, 0.02% NaN₃, and 2mM EDTA) twice. Cells were incubated with FcR blocking reagent plus surface-antibody cocktail for 40 min on ice. After incubation, surface marker-stained cells were washed twice with Cy-FACS buffer. Cells were then fixed with 4% paraformaldehyde for 25 min on ice and permeabilized with permeabilization buffer (Invitrogen, Carlsbad, CA, USA) for 40 min containing the intracellular stain cocktail. All antibodies are listed in the [key resources table](#). Cells were then washed twice with PBS and stained with 200 μ L of DNA intercalator per million cells. Cells were acquired on a CyTOF2 mass cytometer (Fluidigm, South San Francisco, CA, USA) and data were uploaded to Cytobank for further analysis. Events were gated on singlets, live, and CD45⁺ samples. A maximum of 100,000 events were then visualized using a standard UMAP algorithm. Populations of interest were manually gated and verified based on lineage marker expression.

Single-cell RNA sequencing data analysis in humans

Processed count data were downloaded from Gene Expression Omnibus under the following sessions: GSE121636,⁶³ GSE123814,⁶⁴ GSE139555,⁶⁵ GSE145370,⁶⁶ GSE154826,⁶⁷ GSE155698,⁶⁸ and GSE176078.⁶⁹ Ovarian data were downloaded from a code repository.⁷⁰ Expression data were imported into R, v4.1.0 (R Foundation for Statistical Computing, Vienna, Austria) using the Seurat (v4.1.0) R package.⁷¹ Cells were filtered for PTPRC expression to ensure immune cells. Additional quality control filtering was based on the percentage of mitochondrial genes <10% of counts and removal of cells with a feature number greater than 2.5 of the standard deviation of all cells. Myeloid cells were isolated using the scGate (v1.0.0) R package⁷² using the “MoMacDC” model. After isolation, manual removal of monocytes utilized feature counts and canonical markers. Dimensional reduction to produce a UMAP (RunUMAP) utilized the standard Seurat workflow, with the addition of data harmonization (RunHarmony) using the harmony (v0.1.0) R package⁷³ using sequencing run and cancer type as the grouping variables. Both the UMAP calculation and neighbor identification used 15 harmonized dimensions. Single-cell gene enrichment was performed using the UCell implementation⁷⁴ in the escape R package⁶³ across the Hallmark and C2 libraries in the Molecular Signaling Database.⁷⁵ Statistical testing across all cancer types was performed using the Kruskal-Wallis test, with individual comparisons calculated with the pairwise Wilcoxon test. Adjusted p values for significance testing were based on the total number of pairwise Wilcoxon results using the Bonferroni correction for multiple hypothesis testing.

Single-cell RNA sequencing data analysis in mice

Single-cell analysis was performed as previously described.^{59,76} Briefly, PDAC tissues were taken from vehicle-treated, GB1275-treated KP2 subcutaneous pancreatic tumors, and at 14 days post-treatment. Immune cells (CD45⁺) were sorted by an Aria-II cell sorter (BD Biosciences, San Jose, CA, USA). Each sample was generated from a pool of three mice per treatment group, and two total libraries were sequenced.

Sorted cells from each sample were encapsulated into droplets and libraries were prepared using Chromium Single Cell 3'v3 Reagent kits according to the manufacturer's protocol (10 \times Genomics, Pleasanton, CA, USA). The generated libraries were sequenced by a NovaSeq 6000 sequencing system (Illumina, San Diego, CA, USA) to an average of 50,000 mean reads per cell. Cellranger mkfastq pipeline (10 \times Genomics) was used to demultiplex illumine base call files to FASTQ files. Files from samples were demultiplexed with >97% valid barcodes, and >94% q30 reads. Afterwards, fastq files from each sample were processed with Cellranger counts and aligned to the mm10 reference (Version 3.1.0, 10 \times Genomics) to generate the feature barcode matrix.

The filtered feature with barcode matrices were loaded into Seurat as objects. For each Seurat object, genes that were expressed in less than three cells and cells that expressed less than 1,000 or more than 6,000 genes, were excluded. Cells with greater than 10% mitochondrial RNA content were also excluded, resulting in 10,933 cells in the vehicle and 12,086 in the GB1275-treated group. SCTransform with default parameters was used on each individual sample to normalize and scale the expression matrix against the sequence depths and percentages of mitochondrial genes. Cell cycle scores and the corresponding cell cycle phase for each cell were calculated and assigned after SCTransform based on the expression signatures for S and G2/M genes (CellCycleScoring). The differences between the S phase score and G2/M score were regressed out by SCTransform on individual samples. Variable features were calculated for each sample independently and ranked, based on the number of samples they were independently identified (SelectIntegrationFeatures). The top 3,000 shared variable features were used for multi-set canonical correlation analysis to reduce dimensions and identify projection vectors that defined shared biological states among samples and maximized overall correlations across datasets. Mutual nearest neighbors (pairs of cells, with one from each dataset) were calculated and identified as “anchors” (FindIntegrationAnchors). Multiple datasets were then integrated based on these calculated “anchors” and guided order trees with default parameters (IntegrateData). Multiple datasets were then integrated based on using Harmony Integration (RunHarmony). Principle component analysis (PCA) was performed on the 3,000 previously calculated genes (function RunPCA). A UMAP dimensional reduction was performed on the scaled matrix using the first 30 PCA components to obtain a two-dimensional representation of cell states. Then, these defined 30 dimensionalities were used to refine the edge weights between any two cells based on Jaccard similarity (FindNeighbors) and were used to cluster cells through FindClusters functions, which implemented shared nearest neighbor modularity optimization. To characterize clusters, the FindAllMarkers function with log-fold threshold = 0.25 and minimum 0.25-fold difference and MAST test results were used to identify signatures alone with each cluster. Then, the TAMs were selected, and the top 3,000 variable features were recalculated to recluster. DEGs between the two groups were calculated for each dataset with min.pct of 0.1 and logfc. threshold of 0.01 and MAST test (FindMarkers). Then, the differentially expressed gene (DEG) lists from each dataset were filtered with a value of p < 0.05 and ranked based on fold change. These ranked gene sets were fed into GSEA to test for Gene Ontology terms, Kyoto

Encyclopeida of Genes and Genomes pathways, Reactome Database, and the Molecular Signatures Database gene sets with false discover rate (FDR) < 0.05 in ClusterProfiler.⁷⁷

Mouse tissue isolation and flow cytometry

Following tissue digestion, single-cell suspensions were resuspended in flow cytometry buffer (PBS containing 1% BSA), FcR blocked with rat α -mouse CD16/CD32 antibodies (Ebioscience, Santa Clara, CA, USA) for 10 min and pelleted by centrifugation. Where applicable, CD8 $^{+}$ T cells specific for antigen OVA were labeled by incubating cell suspension with H2Kb::SIINFEKL-specific MHC-I dextramer (1:5; Immudex protocol) for 10 min at room temperature prior to extracellular staining. Single cells were consequently labeled with 100 μ L of fluorophore-conjugated α -mouse extracellular antibodies at recommended dilutions for 25 min on ice. Intracellular staining for intracellular markers was conducted subsequently using the EBioscience Transcription Factor Staining buffer set, according to manufacturer's instructions. All antibodies are listed in [key resources table](#). Data were acquired on an X-20 (BD Biosciences) or Cytek Aurora (Fremont, CA, USA) and analyzed using FlowJo software (v10).

For ex-vivo T cell functional (cytokine release) assays, following tissue digestion, primary tumor cell suspensions containing 1 million cells were incubated in 96-well plates with 1 μ M Brefeldin A (Biolegend, San Diego, CA, USA) and 2 μ M Monensin Solution (Biolegend) and 1 \times Stimulation Cocktail (eBioscience) for 6 hours at 37°C and 5% CO₂. After incubation, cells were labeled with fluorophore-conjugated anti-mouse antibodies as described above. For *in vitro* T cell functional assays, following spleen smashing and single-cell suspension procedures, cells were incubated and treated as ex-vivo T cell function assays in the presence of GB1275 at different doses for indicated periods. For *in vitro* T cell proliferation assay, T cells from the spleen were labeled by CFSE (5 μ M, Invitrogen by Thermo Fisher Scientific), and treated with GB1275 at different doses for 2 days. After incubation, cells were labeled with fluorophore-conjugated anti-mouse antibodies as above. Data were acquired on Cytek Aurora and analyzed using FlowJo software (v10).

Immunohistochemistry and mpiHIC

Tissues were fixed in 10% neutral formalin for 24 hours and embedded in paraffin after graded-ethanol dehydration and sectioned into 6- μ m sections using a microtome. Automated staining of tissues was carried out on the BOND RXm (Leica Biosystems, Wetzlar, Germany) following dewaxing and appropriate antigen retrieval. Immunostaining was chromogenically visualized using the Bond Polymer Refine Detection (DS9800, Leica Biosystems). Slides were dehydrated through graded ethanol, followed by xylene, then mounted using xylene-based Cytoseal (Thermo Fisher). Primary antibodies are listed in [\(key resources table\)](#).

For IHC, whole-tissue scans at 10 \times or 20 \times magnification were obtained on a Zeiss Axio Scan Z1 brightfield/fluorescence Slide Scanner. Whole-tissue scans were analyzed with HALO software (Indica Labs, Albuquerque NM, USA) using Area quantification, Cytonuclear, or HighPlex modules.

For mpiHIC of mouse PDACs, embedded tissues were sectioned into 6- um sections and loaded into BOND RXm (Leica Biosystems) for a series of staining, including using antibodies to pSTAT1, STING, p65, CD11b, F4/80, and CK19. Human TMA slides were stained with antibodies to CD8, STING, CD163, CD11b, and CK19. Tumor biopsy slides were stained with antibodies to CD8, STING, pSTAT1, CD163, CD11b, p65, and PanK. Based on antibody host species, default manufacturer protocols were used (IntenseR and Polymer Refine), containing antigen retrieval with citrate buffer, goat serum and peroxide block, primary antibody incubation, post-primary incubation, and chromogenically visualized with an AEC substrate (Abcam, Cambridge, UK). Between every two cycles of staining, the slides were manually stained for hematoxylin, then scanned by Axio Scan.Z1 (Zeiss, Jena, Germany). The slides were then destained by a gradient of ethanol plus a 2% hydrochloride wash and blocked with extra avidin/biotin (Vector Laboratories, Burlingame, CA, USA) and a Fab fragment block (Jackson Laboratory, Bar Harbor, ME, USA). Prior to starting another staining cycle. Citrate-based antigen retrieval was performed before each staining cycle.

For mpiHIC, images of the same specimen, but using different stains, were cropped into multiple segments by Zen software (Zeiss). Each segment was then deconvoluted (Deconvolution, Version 1.0.4; Indica Labs) for individual stains and fused using HALO software with the default manufacturer's settings. Markers of interest were pseudo-colored and quantified using High Plex FL software in HALO software.

Macrophage depletion

To deplete tissue-resident macrophages, 6–8-week-old FVB/NJ mice were treated with three doses of CSF1 neutralizing antibody (clone 5A1; BioXCell, Lebanon, NH, USA) (1mg, 0.5mg, and 0.5mg on days 3, 10, and 17; [Figure 1H](#)) and three doses of clodronate-containing liposomes (Liposoma, Groningen, The Netherlands; 200 μ L/each on days 4, 11, and 18). Control mice were treated with the same doses/volume of IgG (clone HRPN, BioXCell) and control liposomes (or PBS as indicated, Liposoma). On day 0, mice were implanted orthotopically with 100,000 KI cells and then treated with GB1275 as previously described.

Small animal radiation therapy (RT)

Ten days post-tumor implantation, cohorts of mice were randomized into different treatment groups using gross tumor volumes. Mice were given daily fractionated doses of RT for 5 days (6 Gy \times 5) using the Small Animal Radiation Research Platform (SARRP200; Xstrahl Life Sciences). Mice were placed on the irradiation platform one at a time and fitted with a nose cone for isoflurane anesthesia. Cone beam computed tomography (CT) imaging was performed for each individual mouse to pinpoint tumors, and the images were imported into Muriplan and used to select an isocenter. The tumor was then irradiated to 6 Gy using

anterior-posterior-opposed beams using the 10 mm × 10 mm collimator at a dose rate of 3.9 Gy/min. Mice were monitored over 2 weeks for signs of radiation sickness or weight loss. DietGel recovery gel was provided for a 14-day window immediately following radiation therapy in survival studies.

For *in vitro* radiation experiments, an RS2000 160 kV X-ray irradiator using a 0.3mm copper filter (Rad Source Technologies) was used. PDAC cells were irradiated to 8Gy.

Bone marrow transplantation

Six- to eight-week-old C57BL/6 mice were exposed to irradiation dosed at 800Gy (400Gy × 2). Animals were subsequently injected with 5×10^6 bone marrow cells from either WT or STING-null mice. A syngeneic PDAC model was established with these mice after 4 weeks of recovery.

Isolation of bone marrow-derived macrophages

BM-MACs were isolated following the protocol described previously.⁷⁸ Marrow cells were isolated by flushing femurs and tibias from C57BL/6J mice and cultured in DMEM/F12 medium (Lonza, Basel, Switzerland) containing 10% FBS, penicillin/streptomycin (Gibco) and 20 ng/mL macrophage colony-stimulating factor (M-CSF, PeproTech, Cranberry, NJ, USA). After 5 days in culture, adherent macrophages were harvested and seeded on 10 µg/mL fibronectin-coated (Sigma-Aldrich) plates for different experiments. On day 6, macrophages were pretreated with DMEM/F12 medium (Lonza) containing 1% FBS and DMSO or GB1275 (1, 5, or, 10µM dissolved in DMSO for different experiments) for 1 hour followed by removal of the old media. Cells were incubated in DMEM/F12 medium (Lonza) containing 1% FBS or fresh tumor-conditioned media (TCM) (Note: should not be frozen or kept at 4°C for long time periods), containing GB1275 or DMSO at indicated doses for 1, 4, or 6 hours. In the whole process, 20 ng/mL macrophage colony-stimulating factor was always added to the different media. After indicated periods of stimulation, we removed the media, and rinsed the cells with PBS prior to RNA isolation or other experiments.

RNA isolation and real-time PCR

Total RNA was extracted from tissue or cells, using an E.Z.N.A. Total RNA Kit (Omega Bio-tek, Norcross, GA). Complementary DNAs (cDNAs) were synthesized using qScript cDNA SuperMix (QuantaBio, Beverly, MA, USA). Quantitative real-time PCR Taqman primer-probe sets (Applied Biosystems, Waltham, MA, USA) were used (Table S6), and the relative gene expression was determined on an ABI 7900HT quantitative PCR machine (ABI Biosystems) using Taqman Gene Expression Master Mix (Applied Biosystems). The comparative threshold cycle method was used to calculate fold changes in gene expression, which were normalized to the expression of glyceraldehyde-3-phosphate dehydrogenase (GAPDH), TATA-box binding protein (TBP), and/or hypoxanthine phosphoribosyl transferase (HPRT) as reference genes.

Reverse-phase protein array (RPPA)

Cell extracts were lysed using (RIPA) lysis buffer [25mM Tris-HCl pH 7.5, 150mM NaCl, 1% NP-40, 0.5% DOC, 0.1% SDS] supplemented with protease and phosphatase inhibitors (Roche, Basel, Switzerland). Samples were then submitted to the MD Anderson Cancer Center for the RPPA assay (RPPA CORE 11192019_169).

Cytokine assay

Tumor tissues from the KP2-OVA-GFP orthotopic PDAC model were lysed by Procartaplex lysis buffer (Thermo Fisher Scientific, EPX-99999-000) (50µL lysis buffer per 10mg tissue) supplemented with protease and phosphatase inhibitors (Roche). Protein concentration from each sample was adjusted to 5 mg/mL. Supernatants were harvested after different stimulations of BMDMs for 12 hours. IFNβ, CXCL10, CXCL11, and IL-1β from PDAC tissue and IL-1β from supernatants were measured by enzyme-linked immunosorbent assay (ELISA). For tissue, the amount of IFNβ (DY8234-05, R&D Systems, Minneapolis, MN, USA), IL-1β (DY-401, R&D Systems), CXCL10 (BMS6018MST, Invitrogen, Thermo Fisher Scientific), and CXCL11 (EMCXCL11, Invitrogen, Thermo Fisher Scientific) was shown as pg per mg protein in tissue. For supernatants, the amount of IL-1β was normalized by protein levels in its cell lysate.

Western immunoblot and immunoprecipitation (IP)

Cell lysates were harvested using radioimmunoprecipitation assay (RIPA) lysis buffer [25 mM Tris-HCl pH 7.5, 150 mM NaCl, 1% NP-40, 0.5% DOC, 0.1% SDS] supplemented with protease and phosphatase inhibitors (Roche). Protein from supernatant was isolated by methanol and chloroform, and then dissolved by 1% SDS sample buffer. Protein samples were resolved in Tris-glycine sodium dodecyl sulfate/polyacrylamide gel electrophoresis (SDS/PAGE) gels and transferred to polyvinylidene difluoride membranes (Invitrogen). After blocking in 1× TBST buffer with 5% w/v bovine serum albumin (BSA), membranes were probed with primary antibodies against pp65, tp65, plkB, tlkB, STING, pIRF3, tIRF3, pSTAT1 tSTAT1, SIRT3, IFNβ, CXCL10, and β-actin overnight at 4°C (key resources table). Membranes were washed three times in 1× TBST and probed with HRP-conjugated secondary antibody for 1 hour at RT. Membranes were developed with Pierce ECL Western Blotting Substrates (Pierce Chemical, Dallas, TX, USA) and detected using a ChemiDoc XRS+ system (Bio-Rad, Hercules, CA, USA). For immunoprecipitation, cell lysates were incubated with p65 antibody overnight at 4°C followed by incubation in protein A agarose (Cell Signaling Technology, Danvers, MA, USA) for 3 hours. The beads were washed five times with lysis buffer and then used for western immunoblotting.

Isolate released mtDNA

The mtDNA was isolated following a previously described protocol.⁷⁹ Briefly, after different treatments, the cells were lysed by 1% NP40 for 15 min on ice. The lysates were centrifuged at 13,000 rpm for 15 min at 4°C. Supernatants were transferred to the isolated mtDNA. A NucleoSpin Tissue Kit (Takara Bio USA, San Jose, CA, USA) was adopted to purify mtDNA from the cytosolic fraction according to the manufacturer's instructions. After extracting DNA from the cytosolic fraction, real-time PCR was employed to measure cytosolic mitochondrial DNA. The comparative threshold cycle method was used to calculate fold changes in gene expression, which were normalized to the expression of the 18S rRNA reference gene.

Measuring ROS production

Briefly, after different treatments, cells were harvested and incubated with 10 μM 2'-7'-dichlorodihydrofluorescein diacetate (Sigma-Aldrich) in serum-free medium for 20 min at 37°C in the dark. After incubation, samples were washed twice with cold PBS. Data were acquired on an X-20 (BD Biosciences) and analyzed using FlowJo software (Tree Star, Ashland, OR, USA).

Cell proliferation assay

Cell proliferation assays were performed by using the CellTiter96 Non-Radioactive Cell Proliferation Assay (Promega, Madison, WI, USA) according to the manufacturer's instructions. Briefly, 20,000 BMDMs/well were seeded into 96-well plates and incubated overnight. After different treatments, dye solution was added to live cultures for 4 hours at 37°C. Absorbance was measured at 570 nm on a Multiskan GO plate reader (Thermo Fisher Scientific).

In vitro siRNA treatment

Small interfering RNAs (siRNAs) targeting mouse *Rela*, *Sting1*, *Sirt3* and *Tlr9* were purchased from Integrated DNA Technologies (Coralville, IA, USA). Sequences as listed in the Table S6. The siRNA transfections for primary BMDMs were performed using a Mouse Macrophage Nucleofector™ Kit (Lonza, Basel, Switzerland) and Nucleofector™ 2b Device (Lonza) with prewritten program Y-001 for BMDMs following the manufacturer's instructions. RNA and protein from transfected primary cells were harvested 24 hours after the transfections.

Isolation of human CD14⁺ monocyte-derived macrophages

Leukoreduction chambers from normal donors were obtained from the BJH Pheresis Center (Washington University). Human peripheral blood mononuclear cells (PBMCs) were isolated using Dr. Fehniger's laboratory protocol (Washington University). Briefly, chamber eluate was mixed well with PBS containing 1 unit/mL heparin, centrifuged with brakes-off, and the "buffy layer" was isolated. The tube was centrifuged at 1,800rpm for 10min and pellets were incubated in 1× RBC lysis buffer. After subsequent centrifugation at 1,300rpm for 4min, PBMC pellets were resuspended in RPMI media. Human CD14⁺ monocytes were sorted from PBMCs using an EasySep Human CD14 Selection Kit (Stemcell Technologies, Vancouver, Canada) according to the manufacturer's instructions. CD14⁺ monocyte isolation purity of >90% was confirmed by flow cytometry. CD14⁺ monocytes were cultured in RPMI medium containing 10% FBS, penicillin/streptomycin (Gibco, Gaithersburg, MD, USA) and 50 ng/mL macrophage colony-stimulating factor (M-CSF; PeproTech, Waltham, MA, USA) on 10 μg/mL fibronectin-coated plates (Sigma-Aldrich). After 7 days in culture, adherent macrophages were used for different experiments.

Separation of TCM

A total of 10 mL TCM was filled into the top tube of protein concentrators (3,000 molecular weight cut-off; Thermo Fisher Scientific) and centrifuged at 4,600 × g for 1 hour at 4°C until 80%–90% of the solution from the top tube was in the bottom tube. Concentrated proteins (>3,000) were in the top tube, and the metabolites (<3,000) were in the bottom tube. The different fractions of the TCM were diluted to their original volume with media, then used to treat BMDMs.

QUANTIFICATION AND STATISTICAL ANALYSIS

Statistical analyses

All statistical analyses were performed using Prism software (GraphPad, San Diego, CA, USA), with input from a Biostatistics Core expert at Washington University. All data are representative of at least two independent experiments, unless specifically noted. Sample size was precalculated to satisfy power requirements (with >85% confidence) in most experiments and is specified in the figure legends wherever applicable. To accomplish randomization for orthotopic or syngeneic tumor experiments, animals were sorted by a blinded investigator, with tumor sizes in ascending order and then the groups were assigned in descending order. Each group was checked post hoc to verify that there was no statistical difference in average starting tumor size. Data are shown as the mean ± SEM, unless otherwise noted. Statistical tests such as the unpaired parametric Student's *t* test, analysis of variance (Bonferroni multiple comparisons), one sample *t*-test, and Wilcoxon test were used based on the normality of data. For survival analyses, the log-rank (Mantel-Cox) test was used. A value of *p* < 0.05 was considered statistically significant for all studies; n.s denotes not significant.